

# Clinopyroxene/melt trace-element-partitioning in sodic alkaline magmas

Charles Beard<sup>a,\*</sup>, Vincent van Hinsberg<sup>a</sup>, John Stix<sup>a</sup>, Max Wilke<sup>b,c</sup>

<sup>a</sup>*Earth and Planetary Sciences, McGill University, 3450 University Street, Montreal, Québec, H3A 0E8, Canada*

<sup>b</sup>*Institut für Erd- und Umweltwissenschaften, Universität Potsdam, Golm, Germany*

<sup>c</sup>*Chemie und Physik der Geomaterialien, Deutsches GeoForschungsZentrum GFZ, Potsdam, Germany*

---

## Abstract

Clinopyroxene is a key fractionating phase in alkaline magmatic systems, but its impact on metal-enrichment processes, and the formation of REE + HFSE mineralisation in particular, are not well understood. To constrain the control of clinopyroxene on REE + HFSE behaviour in sodic (per)alkaline magmas, a series of internally heated pressure vessel experiments was performed to determine clinopyroxene-melt element-partitioning systematics. Synthetic tephriphonolite to phonolite compositions were run  $\text{H}_2\text{O}$ -saturated at 650–825°C with oxygen fugacity buffered to  $\log f\text{O}_2 \approx \Delta\text{QFM} + 1$  or  $\log f\text{O}_2 \approx \Delta\text{QFM} + 5$ . Clinopyroxene-glass pairs from basanitic to phonolitic fall deposits from Tenerife, Canary Islands, were also measured to complement our experimentally derived data set.

The REE partition coefficients are 0.3–53, typically 2–6, with minima for high-aegirine clinopyroxene. Diopside-rich clinopyroxene ( $\text{Ae}_{5-25}$ ) prefer the

---

\*corresponding author

Email address: [charles.beard@mail.mcgill.ca](mailto:charles.beard@mail.mcgill.ca) (Charles Beard)

MREE and have high REE partition coefficients ( $D_{Eu}$  up to 53,  $D_{Sm}$  up to 47). As clinopyroxene become more Na- and less Ca-rich (Ae<sub>25–50</sub>), REE incorporation becomes less favourable, and both the M1 and M2 sites expand (to 0.79 Å and 1.12 Å), increasing  $D_{LREE}/D_{MREE}$ . Above Ae<sub>50</sub>, both M sites shrink slightly and HREE ( $V^I r_i \leq 0.9 \text{ \AA} \approx \text{Y}$ ) partition strongly onto the M1 site, consistent with a reduced charge penalty for REE  $\leftrightarrow \text{Fe}^{3+}$  substitution.

Our data, complemented with an extensive literature database, constrain a model that predicts trace-element-partition coefficients between clinopyroxene and silicate melt using only mineral major-element compositions, temperature and pressure as input. The model is calibrated for use over a wide compositional range and can be used to interrogate clinopyroxene from a variety of natural systems to determine the trace-element concentrations in their source melts, or to forward model the trace-element evolution of tholeiitic mafic to evolved peralkaline magmatic systems.

*Keywords:* rare earth elements, aegirine, experimental petrology, Canary Islands, phonolite, peralkaline

---

## **1. Introduction**

Sodic clinopyroxene appear to more readily incorporate REE than their calcic equivalents (Marks et al., 2004), but despite fractionation of these minerals, melts in evolved alkaline systems can attain high REE contents, even up to economic levels (Kogarko, 1990; Downes et al., 2005; Marks et al., 2011; Sjöqvist et al., 2013; Goodenough et al., 2016; Möller and Williams-Jones, 2016). Trace-element data may be used to model magmatic processes (Spera and Bohrson, 2001; Troll and Schmincke, 2002; Boudreau, 2004; Xu et al., 2010; Girnis et al., 2013; Mungall and Brenan, 2014), but their interpretation requires precise knowledge of mineral/liquid element-partition coefficients. The approach has been applied to studies of mafic systems and mantle melting processes (Niu, 2004; Workman and Hart, 2005; Foley et al., 2013; Coumans et al., 2016; Peters et al., 2017). However, poor constraints on element-partitioning behaviour in alkaline and peralkaline rocks thus far preclude widespread application in these systems.

Experimental investigations of element-partitioning behaviour in alkali-enriched systems are limited in terms of composition (Wood and Trigila, 2001; Huang et al., 2006), and none yet have explored peralkaline conditions where molar  $(\text{Na}+\text{K})/\text{Al}$  exceeds 1. Additional information has been obtained from natural samples by measuring the concentration ratios of phenocryst–glass pairs from volcanic and intrusive rocks (Larsen, 1979; Wörner et al., 1983; Shearer and Larsen, 1994; Severs et al., 2009; Fedele et al., 2009; Mollo et al., 2016). However, these results may be biased by the presence of melt inclusions, mineral inclusions and mineral zoning, and their interpretation is commonly complicated by unknown or poorly constrained P-T-H<sub>2</sub>O-*f*O<sub>2</sub> con-

<sup>26</sup> ditions of equilibration and assumptions of closed-system behaviour.

<sup>27</sup> In this contribution, we present trace-element-partition coefficients be-  
<sup>28</sup> tween sodic clinopyroxene and silicate melts of tephriphonolite to phonolite  
<sup>29</sup> composition, as determined from internally heated pressure vessel experi-  
<sup>30</sup> ments on synthetic and natural compositions. These are complemented by  
<sup>31</sup> well-constrained natural volcanic phenocryst-glass pairs from Canary Islands  
<sup>32</sup> pyroclastic fall deposits. We characterise the mineral compositional controls  
<sup>33</sup> on element-partitioning behaviour and present a predictive model for clinopy-  
<sup>34</sup> roxene/melt element-partitioning that can be used to generate clinopyrox-  
<sup>35</sup> ene/melt partition coefficients using only clinopyroxene major-element com-  
<sup>36</sup> positions (e.g., as measured by electron-microprobe). This approach permits  
<sup>37</sup> forward modelling of element budgets during differentiation processes in mag-  
<sup>38</sup> matic systems, including evolved sodic alkaline systems, as well as providing  
<sup>39</sup> a mineral-based tool that can be used to reconstruct parental melt composi-  
<sup>40</sup> tions from clinopyroxene compositions in natural rocks.

## <sup>41</sup> 2. Methodology

### <sup>42</sup> 2.1. Experiment starting materials

<sup>43</sup> Clinopyroxene were synthesised in sodic alkaline melts of varying com-  
<sup>44</sup> position to obtain a range of mineral compositions consistent with those in  
<sup>45</sup> natural systems. Starting glass compositions are given in Table 1 and Figure  
<sup>46</sup> S1. Synthetic glasses L1 and L5 were prepared from reagent-grade oxide and  
<sup>47</sup> carbonate powders, ground together in an agate mortar, decarbonated for  
<sup>48</sup> 6 hrs at 450°C, then homogenised in air for 3 hrs at 1400°C in a Pt cru-  
<sup>49</sup> cible. Repeated fusion and grinding in agate ensured chemical homogeneity

50 of the starting glasses, which was confirmed by electron-microprobe analyses  
51 of the final fused glass. Finely-ground Mud Tank zircon was added to the  
52 homogeneous major-element glasses as a source of Zr, Hf, Nb and Ta; the  
53 glasses were then fused for a further three hours at 1400°C. The remaining  
54 trace-elements were added as a cocktail of single element nitrate solutions  
55 (ICP-MS standards), dried onto the powdered glasses, then denitrified at  
56 450°C for 30 minutes. The synthetic basanite L1 and phonolite L5 were  
57 mixed in varying proportions to make the low alkali (L) series of starting  
58 glasses, while dried NaOH and KOH powders were added to make the mid-  
59 dle (M) and high (H) alkali starting glasses. Analyses of glass compositions  
60 L5 and H5, quenched from superliquidus conditions, confirm that Henry's  
61 law was respected (Supplement S1).

62 A well-mixed rock powder from the Nechalacho Layered Suite in Canada  
63 (Möller and Williams-Jones, 2016, Unit NLS-9, sample L09-194-405.5, al-  
64 ternative sample name VM 11-6) was used as experimental starting mate-  
65 rial for a more extreme peralkaline composition. This composition was not  
66 fused prior to loading into experiment capsules, so as to preserve the origi-  
67 nal volatile-element concentrations. An experiment using this material that  
68 was quenched from superliquidus conditions is homogeneous with respect to  
69 major-elements, as determined from electron-microprobe measurements.

70 *2.2. Experimental equipment and procedures*

71 In total, 36 partitioning experiments were conducted in a Harwood-type  
72 internally heated pressure vessel (IHPV) in the HP-GeoMatS laboratory at  
73 the German GeoForschungsZentrum (Table S1). Temperature was measured  
74 with Type-S thermocouples calibrated against the melting point of NaCl

<sup>75</sup> (Borchert et al., 2010, accuracy of  $\pm 5$  °C at 200 MPa). Argon gas was used  
<sup>76</sup> as the pressure medium, and pressure was measured with a strain gauge to  
<sup>77</sup> an accuracy of  $\pm 7$  MPa. During the experiments, pressure was controlled  
<sup>78</sup> automatically and held within  $\pm 5$  MPa of stated values.

<sup>79</sup> Oxygen fugacity was buffered to the intrinsic redox conditions of the  
<sup>80</sup> experimental setup, which corresponds to  $\log f\text{O}_2 \text{ ca. } \Delta\text{QFM} + 1$  in our  $\text{H}_2\text{O}$ -  
<sup>81</sup> saturated charges (see Chou, 1986; Berndt et al., 2002; Jugo et al., 2010). One  
<sup>82</sup> experiment using the Nechalacho Layered Suite composition was performed  
<sup>83</sup> in a double capsule with a haematite solid buffer, designed to increase  $f\text{O}_2$   
<sup>84</sup> and promote crystallisation of  $\text{Fe}^{3+}$ -rich clinopyroxene (Eugster and Wones,  
<sup>85</sup> 1962). This experiment ran at the Hm-Mt buffer, which corresponds to  
<sup>86</sup>  $\log f\text{O}_2 \approx \Delta\text{QFM} + 5$ , as confirmed by presence of both buffer minerals in  
<sup>87</sup> the outer capsule following quench. The experiments were designed to run  
<sup>88</sup> between the liquidus and solidus for each composition, which corresponds to  
<sup>89</sup> temperatures between 650 and 825°C, all at 200 MPa pressure (Table S1).

<sup>90</sup> Powdered starting glass and distilled, deionised water were welded inside  
<sup>91</sup> 3.0 or 3.5 mm outer diameter platinum capsules of 20–25 mm length (see Ta-  
<sup>92</sup> ble S1). To verify that capsules were sealed, they were heated to 110°C and  
<sup>93</sup> weighed before and after. The amount of water sealed inside the capsules  
<sup>94</sup> varied with temperature and composition and was kept in excess of satu-  
<sup>95</sup> ration (Carroll and Blank, 1997; Moore et al., 1998; Schmidt and Behrens,  
<sup>96</sup> 2008). Water saturation was confirmed post-run by puncturing capsules and  
<sup>97</sup> checking for water expulsion and mass loss on drying at 110°C.

<sup>98</sup> The capsules were loaded into the vessel, pressurised to 200 MPa, then  
<sup>99</sup> heated to superliquidus temperatures for at least 16 hrs (Table S1) to per-

mit homogenisation of trace-element concentrations, dissolution of water and equilibration of  $fO_2$  by exchange of  $H_2$  through the capsule wall (cf. Gaillard et al., 2002). Following homogenisation, temperature was lowered to run conditions. An initial set of experiments were cooled rapidly from homogenisation to run temperature at about 100°C/min. A second set of experiments were cooled to run temperature at 1°C/min to promote slow growth of crystals and to minimise the formation of compositional gradients in the melt. Vessel temperature was then cycled between run temperature and run temperature + 10°C to promote dissolution of small crystals at the expense of larger grains, and to promote crystal growth close to the run temperature. Element partitioning results are consistent among experiments of different cooling paths. In all experiments, run temperature was kept constant for at least 40 hrs to allow for chemical homogenisation of melt and growth of crystals via Ostwald ripening. Capsules were then quenched to room temperature.

To minimise the growth of groundmass crystals on cooling, a rapid-quench apparatus was used where possible (Table 2). We have not measured quench rates in this vessel, but the capsules probably cooled at rates of several hundred degrees Celcius per second (e.g. Berndt et al., 2002). For the rest of the experiments, quenching was achieved by cutting power to the furnace, which resulted in cooling to below the glass-transition temperature (< 350°C; Giordano et al., 2005) in less than 150 seconds.

### 2.3. Natural samples

Alkaline volcanism on Tenerife is associated with a weak thermal mantle plume that impinges upon thick, old, slow-moving oceanic lithosphere (Car-

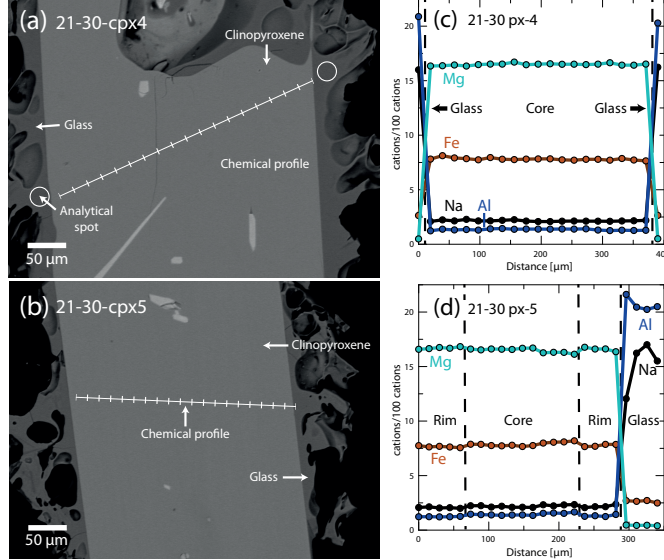


Figure 1: Examples of textural features from Canary Islands clinopyroxene phenocrysts from this study. (a, b) Backscattered electron images show that crystals are euhedral and are free from complex zoning patterns. (c, d) Chemical profiles across clinopyroxene phenocrysts and glass rims (quenched melt), as measured by wavelength dispersive spectroscopy, showing that zoning is effectively absent in these clinopyroxene. In (c) analyses of glass are aligned with the chemical profile shown in (a). Glass analyses shown in (d) are from rims of quenched melt from other clinopyroxene phenocrysts recovered from the same pumice sample. Both pictured phenocrysts are from the basal air fall deposit, associated with the ~2 ka eruption of Pico Viejo, Tenerife (Ablay et al., 1995).

racedo et al., 2007). This geological scenario has favoured development of a complex magma-plumbing system that produces a great diversity of volcanic products from alkali basalt to phonolite in composition. The Las Cañadas edifice, a large, central, composite stratovolcano (Bryan et al., 1998; Brown et al., 2003; Edgar et al., 2007), rests upon a base of at least three mafic al-

<sup>130</sup> kaline shield volcanoes (Thirlwall et al., 2000; Guillou et al., 2004; Gurenko  
<sup>131</sup> et al., 2006). Xenoliths indicate that a nepheline syenite intrusive system  
<sup>132</sup> underlies the island (Wiesmaier et al., 2012).

<sup>133</sup> Six clinopyroxene/glass pairs from four different volcanic eruptions on  
<sup>134</sup> Tenerife have been investigated. The  $\sim 2$  ka eruptive products of Montaña  
<sup>135</sup> Blanca and Pico Viejo (Abhay et al., 1995) are phonolitic, plinian fall de-  
<sup>136</sup> posits, whereas Montaña Samara is a monogenetic, mafic cinder cone (Albert  
<sup>137</sup> et al., 2015). Phase-equilibrium experiments conducted on Montaña Blanca  
<sup>138</sup> unit UMB-II suggest that magma was stored prior to eruption at  $850 \pm 15^\circ\text{C}$ ,  
<sup>139</sup>  $50 \pm 20$  MPa, with  $2.5 \pm 0.5$  wt% H<sub>2</sub>O at  $\log f\text{O}_2 \approx \text{NNO} - 0.5$  (Andújar and  
<sup>140</sup> Scailet, 2012). Field locations, mineral proportions and major-element com-  
<sup>141</sup> positions of the clinopyroxene and glasses are presented in Table S1.

#### <sup>142</sup> 2.4. Sample preparation

<sup>143</sup> Experiment capsules were torn open with pliers, and charges were split  
<sup>144</sup> using a low-speed wafering saw. Samples were mounted in epoxy resin and  
<sup>145</sup> polished for *in-situ* chemical analyses.

<sup>146</sup> Natural pyroclastic rocks were rinsed in tap water and crushed with a  
<sup>147</sup> hammer. Crystals and glass fragments, hand-picked from a sieved size-  
<sup>148</sup> fraction between 1.18 mm and 125  $\mu\text{m}$ , were used to make grain mounts  
<sup>149</sup> containing 5–20 crystals of clinopyroxene per sample. Natural samples also  
<sup>150</sup> contain biotite, sanidine,  $\pm$  spinel, amphibole, olivine, titanite and sodalite.  
<sup>151</sup> Clinopyroxene mineral mounts were examined using backscattered electron  
<sup>152</sup> imaging to select euhedral crystals that were free from melt inclusions and  
<sup>153</sup> chemical zoning ( $n = 6$ , Fig. 1).

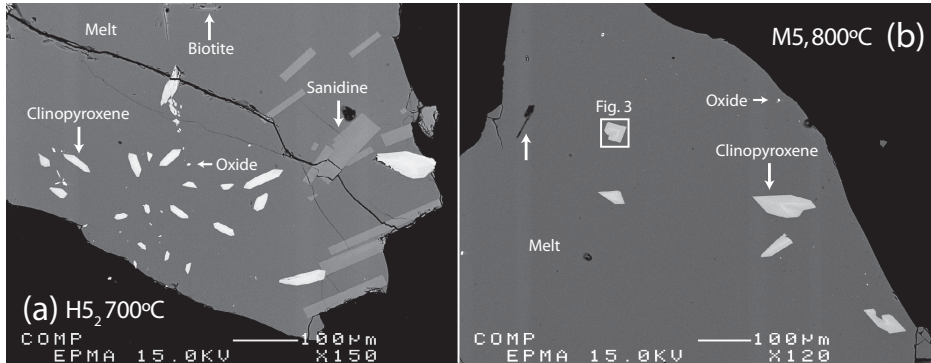


Figure 2: Backscattered electron images showing typical textures of run products from the internally heated pressure vessel experiments. Crystal fractions are typically small (<10% by area), with blade-shaped, euhedral clinopyroxene and glasses free of quench crystals.

<sup>154</sup> **3. Analytical techniques**

<sup>155</sup> All experimental products were examined by reflected-light optical mi-  
<sup>156</sup> croscopy and scanning electron microscopy, and all phases produced were  
<sup>157</sup> identified by electron-microprobe using an energy-dispersive detector. Im-  
<sup>158</sup> ages were obtained to estimate modal proportions of phases, which were  
<sup>159</sup> calculated using ImageJ freeware (Rasband, 2016, see Table S1).

<sup>160</sup> *3.1. Electron-microprobe analysis*

<sup>161</sup> Major-element compositions of experimental products and natural min-  
<sup>162</sup> erals and glasses were measured with a JEOL 8900 instrument at McGill  
<sup>163</sup> University and a JEOL 8230 instrument at the University of Ottawa (Table  
<sup>164</sup> 3). An accelerating voltage of 15 kV was used with a 15 nA beam of 5  $\mu\text{m}$   
<sup>165</sup> diameter for minerals, and a 4 nA beam of 50  $\mu\text{m}$  diameter for glasses. Count  
<sup>166</sup> times for all elements were 60 sec. Using the above routine, we observed no  
<sup>167</sup> sodium loss over the measurement time period. For the silicate minerals and

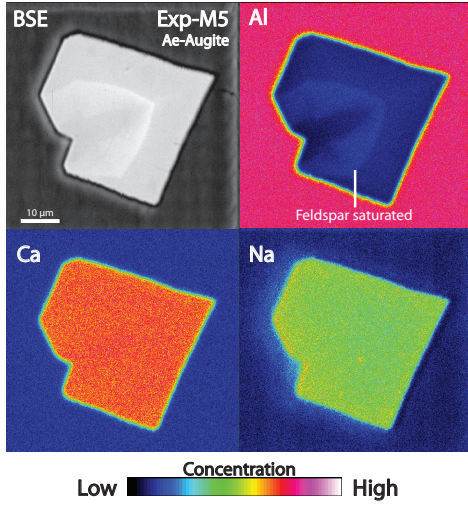


Figure 3: Element maps of clinopyroxene from internally heated pressure vessel experiment M5 (see box in lower magnification image, Fig. 2b). Aegirine-augite clinopyroxene have a sharp internal boundary that reflects feldspar saturation and are subtly zoned. Further element maps are available as an electronic supplement (Fig. S3).

<sup>168</sup> glasses, both synthetic and natural minerals or oxides were used for calibration  
<sup>169</sup> (see Table S1). Analytical uncertainties were determined by multiple  
<sup>170</sup> analyses of reference materials and duplicate analyses of samples.

<sup>171</sup> Element distribution maps were generated with a JEOL 8900 instrument  
<sup>172</sup> at McGill University using an accelerating voltage of 15 kV, a focussed 40  
<sup>173</sup> nA beam, and a dwell time of 50 ms per pixel (Figs. 3, S3). Fe, Ti, Al, Si  
<sup>174</sup> and Na were measured with wavelength-dispersive detectors, while Ca and  
<sup>175</sup> Mg were measured with an energy-dispersive spectrometer.

<sup>176</sup> Transects of Ce, Mg and Fe concentrations within the experiment clinopy-  
<sup>177</sup> roxene were measured with a JEOL 8900 instrument at McGill University  
<sup>178</sup> using a focussed beam of 50 nA with an accelerating voltage of 20 kV. Ce was

179 counted with a wavelength-dispersive spectrometer with an LIFH crystal for  
180 100 sec (MAC-Ce standard). Mg and Fe were counted for 20 sec, with TAP  
181 and LIF crystals respectively (diopside and olivine standards, respectively).  
182 Matrix corrections for Mg, Fe and Ce were not possible with these data, for  
183 lack of other major-elements measured, however their relative values may  
184 still be used to assess the extent to which the clinopyroxene are chemically  
185 zoned.

186 *3.2. Laser-ablation ICP-MS*

187 Trace-element concentrations of clinopyroxene and glasses were deter-  
188 mined by laser-ablation ICP mass-spectrometry. Analyses were performed  
189 at McGill University using a NewWave 213 nm Nd-YAG laser system coupled  
190 to a Thermo Finnigan iCAP-Qc quadrupole ICP-MS instrument. Typical flu-  
191 ence was 3–12 J/cm<sup>2</sup> (from 80 μm to 8 μm spot sizes), with a repetition rate  
192 of 10 Hz. Ablated material was transferred to the ICP-MS in a He flow of 800  
193 mL/min and mixed with Ar prior to injection into the plasma. Instrumental  
194 drift was monitored by repeat analyses of the primary standard glass BCR-  
195 2G, with bias monitored by repeat analyses of secondary standards UTR-2  
196 peralkaline rhyolite and USGS-RGM-1 rhyolite glasses (Table S1). Sample  
197 surfaces were pre-ablated to remove residues from polishing materials and to  
198 improve ablation efficiency.

199 Primary and secondary standards and an unzoned Canary Islands clinopy-  
200 roxene were analysed with beam sizes of 8–80 μm to monitor crater-size-  
201 dependent element-fractionation effects; none were found for the elements  
202 reported here. For minerals and glasses in the experimental charges, beam  
203 sizes of 8–40 μm and 16–80 μm were used, respectively. Depending on grain-

204 size and availability, 5–14 mineral grains and 3–10 areas of glass were anal-  
205 ysed per charge. Natural clinopyroxene and rim glasses were analysed using  
206 a beam size of 12–80  $\mu\text{m}$  and 12–30  $\mu\text{m}$ , respectively. Wherever possible,  
207 ablation was performed along lines parallel to crystal rims (1–3  $\mu\text{m} / \text{sec}$ ).

208 Drift corrections and data reduction were conducted in Iolite v2.5 (Paton  
209 et al., 2011). The total of major-elements measured by LA-ICP-MS or, where  
210 available, the Al concentration from electron-microprobe analyses, was used  
211 as an internal standard (Table 3). For some experiments, ablation through  
212 the minerals was too rapid to generate a stable signal for data-reduction  
213 purposes. In these cases, a mixing model was applied to estimate the com-  
214 position of these clinopyroxene, similar to those applied by Rubatto and  
215 Hermann (2007); Yang et al. (2018)(see supplementary methods S5).

## 216 4. Results

### 217 4.1. Run product phase stability and crystallinity

218 Trace-element partition-coefficients are reported for eleven experimental  
219 charges. 25 additional experiments were rejected as their run temperatures  
220 were superliquidus or subsolidus, or because their growth textures were in-  
221 dicative of disequilibrium (e.g. Fig. S3). Phase proportions are provided in  
222 Table S1.

223 All reported experimental runs were near-liquidus (3–22% crystals, RL  
224 images) and are characterised by a homogeneous distribution of phases (Fig  
225 2), except for experiments H5<sub>3</sub> and NLS-9<sub>2-HM</sub>, in which sanidine crystals  
226 are concentrated at the centre. Glasses are clean, homogeneous and show a  
227 limited range of major- and trace-element compositions for each experiment

(Fig. S1). Clinopyroxene crystals are generally small, euhedral blades with a narrow range of sizes for a given experiment (<10  $\mu\text{m}$  to 100  $\mu\text{m}$  in cross section, Figs. 2–3). In addition to clinopyroxene and glass, experiments on mafic to intermediate compositions produced magnetite, titanite  $\pm$  kaersutite amphibole, whereas some phonolitic experiments produced biotite, alkali feldspar  $\pm$  magnetite (Table S1).

Constraining the full phase equilibria of all of the investigated compositions was beyond the scope of this study. Run conditions and run products given in Supplement S1 provide insight into phase equilibria that might guide future studies. In our experiments it can be seen that clinopyroxene has a wide stability field across the investigated physicochemical conditions, with only a single starting composition generating amphibole in place of pyroxene (experiments L3 and L3<sub>2</sub>).

#### 4.2. Glass compositions

All run-product glasses are homogeneous across the length and breadth of the experiment capsules based on multiple electron-microprobe and laser-ablation ICP-MS analyses. Most major-element oxide compositions, as measured by electron-microprobe, show relative standard deviations of < 5% within experiment capsules, with minor-elements oxides (concentration < 1%) showing greater variability, most with standard deviations between 5 and 10 % relative. Trace-element-compositions of the glass, as measured by laser-ablation ICP-MS, typically show time-weighted relative standard deviations of 1 to 8% within each capsule, with this variability depending on both the absolute concentration of that element and on the beam-size that was used for analyses (Supplement S1). Low sum-totals of major-element

253 oxide concentrations in the electron-microprobe analyses are a result of high  
254 dissolved-water contents in the quenched melt.

255 On a total-alkalies vs. silica diagram the experiment glasses are predom-  
256 inantly phonolitic in composition, though span the trachyte-phonolite join  
257 (Fig. S1). Their alkalinity index (molar  $(\text{Na} + \text{K})/\text{Al}$ ) is 0.85 to 1.40, cross-  
258 ing the alkaline–peralkaline join, and the Mg# of these quenched melts is 0  
259 (Mg-free) to 22. The dissolved water content of these quenched melts is 8.8  
260 to 10.7 wt.% (by difference method from EPMA data, with the Fe oxidation  
261 state assigned following Kress and Carmichael 1991) and their NBO/T ratios  
262 are 0.98 to 1.42 (Mysen et al., 1982, 1985). The halogen content of the syn-  
263 thetic experiments is nominally zero, whereas glasses from the Nechalacho  
264 Layered Suite composition experiments typically contain 0.1 % F and 0.02  
265 % Cl by weight.

266 The Canary Islands glasses are trachytic to phonolitic (CHECK) and are  
267 alkaline to weakly peralkaline in composition (alkalinity index of 0.78 to 1.16)  
268 with Mg# of 8 to 39. Dissolved water content and NBO/T ratios are not  
269 reported for these glasses because of post-eruptive loss of volatiles. These  
270 Canary Islands glasses typically contain 0.2 % F and 0.4 % Cl by weight.

271 **To add: a more comprehensive figure showing glass composi-**  
272 **tions. This could be in the main text, or as a supplement. Added**  
273 **TAS, MgO vs. CaO and AI vs Mg#.** (Made, but need Mac for  
274 **figure symbols.)**

275 *4.3. Compositions of the clinopyroxene and major-element exchange*

276 The Canary Islands clinopyroxene are diopside ( $\text{Di}_{60-90}, \text{Ae}_{3-20}$  CHECK)  
277 in composition, with most crystals containing about 0.05 c.f.u.  $^{IV}\text{Al}$  (in the

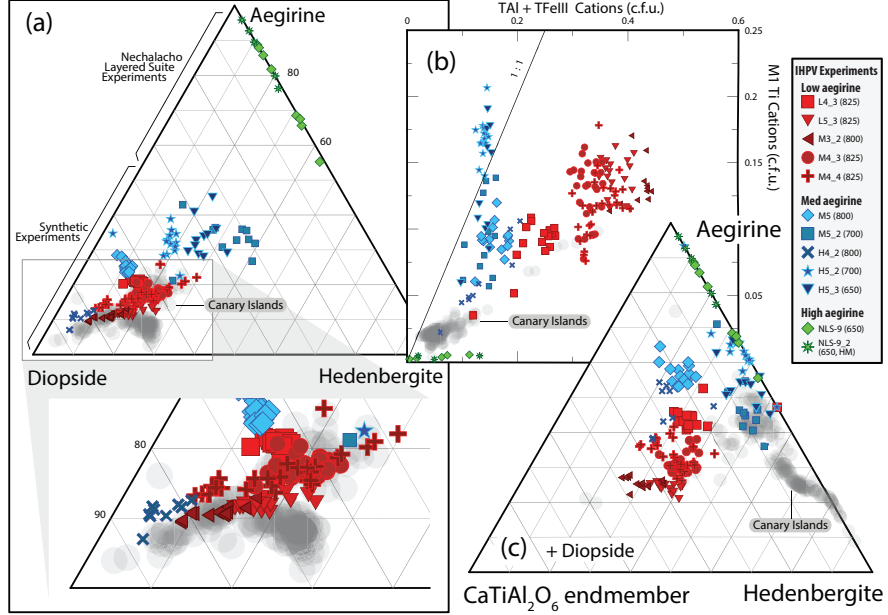


Figure 4: Clinopyroxene grown in internally heated pressure vessel experiments (a) expressed in terms of diopside, hedenbergite and aegirine end-members, (b) their M1Ti and tetrahedral Al and Fe<sup>3+</sup> contents, and (c) expressed in terms of aegirine, hedenbergite and the theoretical CaTiAl<sub>2</sub>O<sub>6</sub> end-member (Akasaka and Onuma, 1980). Clinopyroxene compositions from Canary Islands volcanic rocks are shown for comparison (this study). Fe<sup>2+</sup>/Fe<sup>3+</sup> within the clinopyroxene was assigned following Droop (1987), then site occupancies and end-member proportions were allocated following Morimoto (1989). For methods used in calculation of the end-member proportions see Supplement S5. The range of clinopyroxene compositions within each experiment records changes to the composition of the melt during crystal growth, whereby the cores of the crystals record the first stage of crystallisation and the rims (highest Fe, Na) are in equilibrium with the quenched melt. **to finish! Also re-plot with a separate symbol to signify Canaries compositions that were used for the derivation of partition coefficients**

278 T site) and 0.02 c.f.u. <sup>VI</sup>Ti (in the M1 site, Tables 3 and S1, Fig. 4). Ex-  
 279 periments on the synthetic compositions produced clinopyroxene of diopside

to aegirine-augite composition, a subset of which overlap with the compositional space defined by the Canary Islands clinopyroxene on a diopside-hedenbergite-aegirine ternary diagram (Fig. 4a). This low-aegirine group of synthetic clinopyroxene display a positive correlation between  $^{IV}\text{Al}$  and  $^{VI}\text{Ti}$  content (red, *low aegirine*,  $\text{Ae}_{5-25}$ ), and notably contain both of these elements at elevated concentration relative to the Canary Islands clinopyroxene ( $^{IV}\text{Al} = 0.20\text{--}0.45$  c.f.u.,  $^{VI}\text{Ti} = 0.07\text{--}0.17$  c.f.u.). A further subset of synthetic clinopyroxene have higher aegirine content (blue, *med aegirine*,  $\text{Ae}_{25-50}$ ) and show a similar range of Ti content to the low aegirine synthetic minerals (0.05–0.18 c.f.u.), but a limited range of lower  $^{IV}\text{Al}$  content (0.1–0.2 c.f.u., Fig. 4b). Experiments performed on the Nechalacho Layered Suite composition (NLS-9, NLS-9<sub>2-HM</sub>, green, *high aegirine*,  $\text{Ae}_{55-95}$ ) reproduced the aegirine-augite to aegirine clinopyroxene from the natural system (Möller and Williams-Jones, 2016) that contain low concentrations of  $^{IV}\text{Al}$  (up to 0.14 c.f.u.) and almost no Ti or Mg.

The Canary Islands clinopyroxene that were selected for determination of mineral–melt partition coefficients are free from melt inclusions, suggesting relatively slow rates of crystal growth (Kennedy et al., 1993, Fig. 1). Chemical zonation, if present, is of a similar magnitude to the analytical precision of our electron microprobe, indicating that pressure, temperature and melt composition remained stable during crystal growth. In the case of these Canary Islands clinopyroxene, the entire mineral is interpreted to be in chemical equilibrium with the adhered quenched melt. Trace-element abundances within these Canary Islands clinopyroxene show core-to-rim variations of about 1–5 % relative, with larger variations in element abundance asso-

305 ciated with sector zoning than with concentric growth zoning (Supplement  
306 S1). (TO CONFIRM with images)

307 By contrast our experiment clinopyroxene display systematic composi-  
308 tional variation between their cores and rims; this variation recording changes  
309 to melt composition during growth of these crystals (e.g. Fig. 3). The sys-  
310 tematics of crystal-chemical zonation both within individual experimental  
311 charges and within groups of experiments reveal major-element exchange  
312 vectors between the clinopyroxene and the melt. Three major-element ex-  
313 change mechanisms correspond to the low (Ae<sub>5–25</sub>), medium (Ae<sub>25–50</sub>) and  
314 high (Ae<sub>55–95</sub>) aegirine domains defined above (Figs. 4b, 5 and S4).

315 **And may be used to infer.... the composition of the mineral  
316 assemblage that is crystallising? To discuss. Comments, please!**

317 With increasing alkali content, the Si content in clinopyroxene increases  
318 at the expense of tetrahedrally co-ordinated Al and Fe<sup>3+</sup>. As aegirine content  
319 increases, substitutions at the tetrahedral site become relatively less impor-  
320 tant than exchanges at the M1 and M2 sites. At the M1 site, the substitution  
321 of Ti for ions of 2+ and 3+ valence correlates well with the exchange of tetra-  
322 hedrally coordinated 3+ cations for Si<sup>4+</sup>. The exchange behaviour of 2+ and  
323 3+ cations at the M1 site depends on the aegirine content of the clinopy-  
324 roxene. In low-aegirine clinopyroxene, the concentration of 3+ ions at the  
325 M1 site is negatively correlated with  $X_{Na}^{M2}$ , whereas in medium- and high-  
326 aegirine clinopyroxene, the M1 site takes progressively more 3+ ions as  $X_{Na}^{M2}$   
327 increases. Substitutions of Ca<sup>M2</sup> for Na<sup>M2</sup> are relatively unimportant in low-  
328 aegirine clinopyroxene, but play a large role in medium- and high-aegirine  
329 exchange vectors.

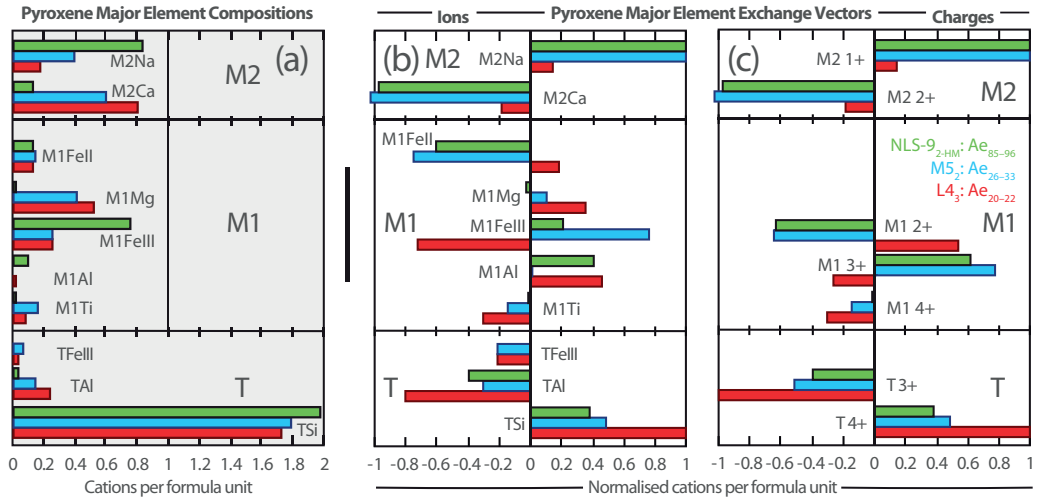


Figure 5: Bar charts showing clinopyroxene composition and major-element exchange mechanisms for three experiments representative of high (green), medium (blue) and low-aegirine (red) clinopyroxene. (a) clinopyroxene major-element compositions are expressed as cations per six-oxygen formula unit (b) exchange mechanisms grouped by ions, (c) grouped by charges. Methods used to calculate these exchange mechanisms are available in the caption of Supplementary Figure S4.

330 Suites of Canary Islands clinopyroxene follow similar major-element ex-  
 331 change systematics to our low aegirine experiment clinopyroxenes (CHECK,  
 332 expand if necessary).

#### 333 4.4. Trace-element concentrations in the experiment clinopyroxene

334 Assessing the homogeneity of trace-element-concentrations within miner-  
 335 als is important when defining equilibrium partition-coefficients because only  
 336 the rims record true chemical equilibrium with the adjacent melt. Measure-  
 337 ments of trace-element-concentrations in experimentally-grown minerals are  
 338 often challenging as a result of their small size; They are commonly compara-

ble in scale to the beam-size of laser-ablation or SIMS systems ( $\sim 10\text{--}20 \mu\text{m}$ ).  
In many cases it is therefore not possible to assess the extent to which trace-element-concentrations are zoned within experimentally-grown crystals. To assess the extent to which trace-element-concentrations are zoned within our experiment clinopyroxene, electron-microprobe transects were measured across seven crystals for the elements Mg, Fe and Ce (Supplement S3). Transects were made across grains from three experiments, each crystallised to varying degrees.

The electron-microprobe transects reveal that clinopyroxene Ce-concentration follows both sector-zoning and concentric growth-zoning patterns, as recorded by backscattered electron images and the XMg of the clinopyroxene. Sector-zoning has a more pronounced effect on the Ce-concentration in the clinopyroxene than concentric growth-zoning, causing one transect to appear ‘laterally-zoned’ and another to appear ‘reverse-zoned’ in terms of Ce-concentration. These effects are due to sector-zoning, with bright sector-zones on BSE images associated with higher Ce-concentrations than dark zones. To gain insight into the variation in clinopyroxene Ce-concentration associated with concentric growth-zoning, analyses were grouped *per-experiment* to average this sector-zoning effect. Ratios of median average Ce-counts / rim Ce-counts represent the difference between the composition of the bulk crystal, as analysed by LA-ICP-MS, and the composition of the clinopyroxene rims that approach chemical equilibrium with the adjacent quenched melt and have a mean value of 1.08, ranging between 1.04 and 1.12. The highest values are found for the largest clinopyroxene crystals and in these, because of their size, we were able to avoid the cores in the analyses via LA-ICP-MS, reducing the

<sup>364</sup> growth-zonation bias in trace-element partition-coefficients.

<sup>365</sup> Where large clinopyroxene crystals were present and time-averages of el-  
<sup>366</sup> ement counts could be used for the reduction of laser-ablation data, trace-  
<sup>367</sup> element-compositions are similar among clinopyroxene crystals within indi-  
<sup>368</sup> vidual experiments (Fig. TO ADD? Table S1) indicating that trace-element  
<sup>369</sup> concentrations in the melt phase remained spatially homogeneous through-  
<sup>370</sup> out the duration of the experiments. Typical trace-element concentrations in  
<sup>371</sup> the experiment clinopyroxene are illustrated in Supplementary Figure S5c.

372 **5. Discussion**

373 *5.1. Attainment of equilibrium in the Canary Islands rocks*

374 The Canary Islands trace-element partition-coefficients presented here  
375 were determined from euhedral, blade-shaped crystals free of melt inclu-  
376 sions and chemical zonation. The corresponding quenched melt was in direct  
377 contact with these crystals and shows no zonation in backscattered electron  
378 images (Fig. 1). While equilibrium conditions are challenging to confirm for  
379 a natural volcanic system, the euhedral forms, chemical homogeneity of crys-  
380 tals, and congruency between samples from separate eruptions suggest that  
381 the crystals grew in a stable environment, and were not subject to chemical  
382 or physical perturbations during growth (Fig. 6).

383 *5.2. Chemical heterogeneity and approach to equilibrium during the experi-  
384 ments*

385 During our experiments crystals of clinopyroxene were grown directly  
386 from unseeded glasses and the run temperature was approached from su-  
387 perliquidus. No attempts were made to reverse these experiments by re-  
388 equilibrating crystals and liquids with deliberately mismatched trace-element  
389 concentrations because of sluggish diffusion of most elements through the  
390 clinopyroxene structure (Van Orman et al., 2001; Zhang et al., 2010). Some  
391 consideration is therefore required before the proximity to chemical equilib-  
392 rium can be established. Further information on the equilibration of these  
393 experiments is in Section 9.

394 A necessary condition for equilibrium is chemical homogeneity within  
395 all measured phases. Except for some sector and concentric zonation within

396 clinopyroxene, major- and trace-element concentrations are generally uniform  
397 in both the quenched melt and the mineral phases. A variety of effects related  
398 to crystal growth may have affected the proximity to which equilibrium was  
399 approached during the experiments:

400 (a) During rapid crystallisation, disequilibrium kinetics may cause major-  
401 and trace-elements to be incorporated into minerals at non-equilibrium con-  
402 centrations (Lu et al., 1995). In the case of clinopyroxene-melt element  
403 partitioning in alkali-silicate systems, experiments demonstrate that rapid  
404 cooling rates (up to 50 °C / hr) result in depletions of Si, Ca and Mg in  
405 the clinopyroxene that are compensated for by enrichments in Al, Na and  
406 Ti (Mollo et al., 2013). Trace-element partitioning systematics determined  
407 from these same experiments are consistent with slowly-cooled experiments  
408 once crystal-chemical ( $^{IV}\text{Al}$ ) systematics are accounted for (ibid. their Fig.  
409 9). Deviations of the partition coefficient of several orders of magnitude can  
410 occur only when small portions of a diffusive boundary layer become incor-  
411 porated into the mineral phase as melt inclusions (Kennedy et al., 1993).

412 (b) Compositional zoning in mineral phases may occur when crystal  
413 growth rates are high relative to diffusion within that crystal phase. In  
414 concentrically-zoned minerals, compatible element concentrations are higher  
415 than equilibrium values in the cores of crystals. Therefore preferential sam-  
416 pling of the rims of concentrically-zoned minerals returns apparent parti-  
417 tion coefficients that more closely approximate equilibrium conditions. At  
418 low-degrees of crystallisation apparent partition coefficients for incompatible  
419 elements are more subtly offset from equilibrium values than those for com-  
420 patible elements because their concentration in the melt is more consistent

421 during crystallisation (Section 9).

422 Having recognised that equilibrium *sensu stricto* was not demonstrated  
423 by our experimental charges, slow diffusion in the clinopyroxene emerges as  
424 the primary cause of chemical heterogeneity, and thus the largest potential  
425 source of bias to our derived partition coefficients. We quantify the departure  
426 from chemical equilibrium with Ce-transects measured across some experi-  
427 ment clinopyroxene via EPMA, with Ce as a proxy for the other compatible  
428 elements (Supplement S1). Concentric growth-zoning has a smaller effect  
429 on clinopyroxene Ce-concentration than sector zoning, the latter of which  
430 was cancelled by averaging transects across several grains per experiment.  
431 Apparent clinopyroxene–melt partition coefficients for compatible elements  
432 (median Ce) are offset from equilibrium (rim Ce) to higher values by 4–8%  
433 (Supplement S1). Large systematic errors outside of these figures are un-  
434 likely because sets of trace-element partition-coefficients of common valence  
435 define Ounma parabolae, discounting the presence of melt-inclusions within  
436 the experiment clinopyroxene (see Fig. 9 below and Kennedy et al., 1993).

437 A 4–8% systematic positive bias in compatible element partition coeffi-  
438 cients is small relative to the variation within our sample set, as well as within  
439 literature values. Furthermore, many of our experimentally-derived partition  
440 coefficients define trends with clinopyroxene major-element composition that  
441 are continuous throughout a set of literature data (Fig. 7 below). For these  
442 reasons, no correction factor has been applied to our data presented in the  
443 figures below, or in Tables 4 and S1.

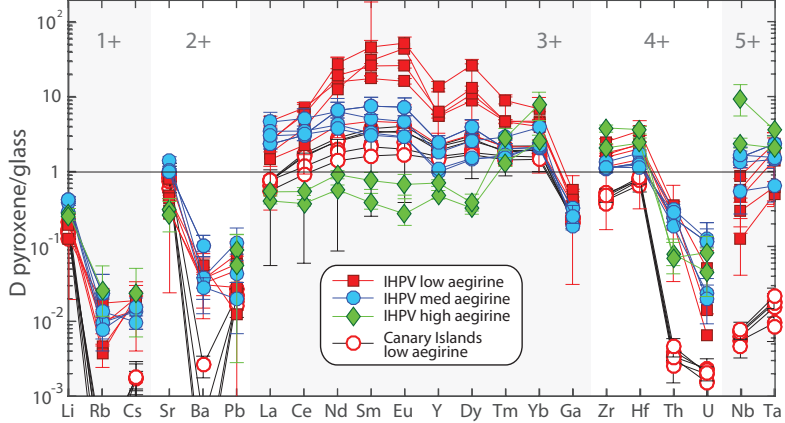


Figure 6: Trace-element partition-coefficients between clinopyroxene and silicate melt, as determined from internally heated pressure vessel experiments ( $n = 11$ ; low-, medium- and high-aegirine types) and from clinopyroxene-rim glass pairs from pyroclastic fall deposits from Tenerife, Canary Islands ( $n = 6$ ; low-aegirine type). Uncertainties on the partition coefficients are at the  $1\sigma$  level.

### 444 5.3. Trace-element-partitioning

445 Trace-element partition-coefficients and their uncertainties were calcu-  
 446 lated as mass concentration ratios between clinopyroxene and coexisting glass  
 447 and are reported in Tables 4 and S1.

448 Where trace-element-concentrations in clinopyroxene could be determined  
 449 using regular time-averages of counts from the ICP-MS system, a time-  
 450 weighted average composition of clinopyroxene was used with that of the  
 451 coexisting glass to calculate trace-element partition-coefficients and their as-  
 452 sociated uncertainty. Where the laser-ablation unmixing model was required  
 453 for reduction of clinopyroxene trace-element analyses, the partition coef-  
 454 ficients were calculated using time-weighted average compositions of glass  
 455 alongside the corresponding ‘unmixed’ clinopyroxene trace-element concen-

456 tration. Because a robust-regression data reduction scheme was used, this  
457 technique returns a median-average trace-element concentration for clinopy-  
458 roxene, whilst effectively rejecting outlier data, for example from the ablation  
459 of minerals other than clinopyroxene that may have been hidden below the  
460 polished surfaces of the grain mounts. Uncertainty calculations are described  
461 in the caption for Figure S5.

462 Three markedly different behaviours of rare earth element partitioning are  
463 observed in the experiments (Fig. 6). These depend on the aegirine concen-  
464 tration in the clinopyroxene and match the major-element exchange vector  
465 domains discussed above. Low-aegirine experiment clinopyroxene ( $Ae_{5-25}$ )  
466 prefer the MREE; medium-aegirine clinopyroxene ( $Ae_{25-50}$ ) show a similar  
467 behaviour, save for higher LREE partition coefficients, whereas high-aegirine  
468 clinopyroxene ( $Ae_{55-95}$ ) strongly prefer HREE and show incompatible be-  
469 haviour for the light and middle REE. The experiment REE partition co-  
470 efficients are 0.3–53, typically 2–6, with minima for LREE and MREE in  
471 high-aegirine clinopyroxene (Fig. 6). Our experimental partition coeffi-  
472 cients are about an order of magnitude higher than in most other studies  
473 of clinopyroxene-melt element-partitioning that were performed on different  
474 bulk compositions (Fig. 7d,e,f), with the exception of high Si systems, such  
475 as the Bandelier Tuff (cf. Olin and Wolff, 2010).

476 The Canary Islands clinopyroxene show similar rare-earth-element partitioning-  
477 systematics to the low-aegirine experiment clinopyroxene, with absolute val-  
478 ues for these partition coefficients of about one order of magnitude lower.

479 The high field-strength elements (HFSE) Zr, Hf, Nb and Ta are compati-  
480 ble to slightly incompatible in the experimental clinopyroxene, and typically

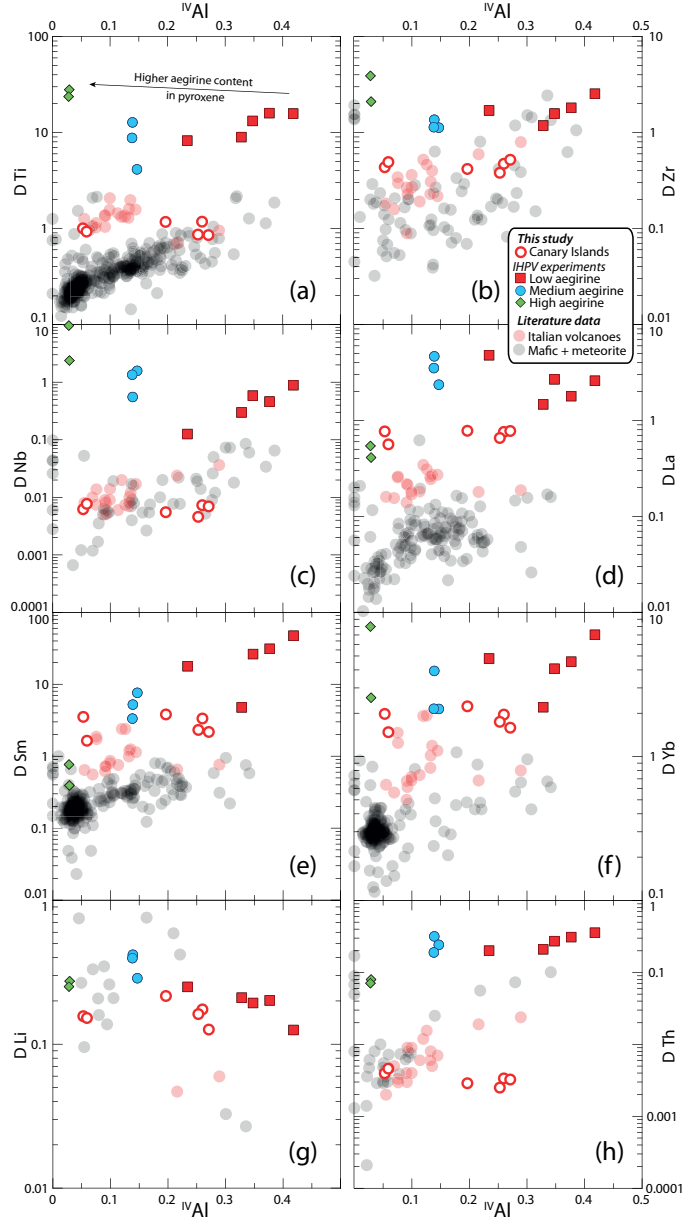


Figure 7: Element partition coefficients for HFSE (Ti, Zr, Nb), REE (La, Sm, Yb) and TE (Li, Th) vs.  $^{IV}\text{Al}$ . Literature values ( $n = 411$ ), including those from the Roman Province, Italy, are from the compilation of Bédard (2014), with additional, more recent, data from Mollo et al. (2016). A similar diagram with  $X_{\text{Na}}^{M2}$  in place of  $^{IV}\text{Al}$  is in Supplement S6.

481 1–2 orders of magnitude less compatible in the Canary Islands clinopyrox-  
482 ene (Fig. 7a,b,c). The HFSE are most compatible in sodic clinopyroxene.  
483 Partition coefficients for the large-ion lithophile elements K, Sr, Pb are pos-  
484 itively correlated with  $X_{Na}^{M2}$  in the low- and medium-aegirine clinopyroxene,  
485 but are lower in high-aegirine clinopyroxene (Fig. S6). The Rb, Cs and Ba  
486 partition coefficients have a high uncertainty and are maximum estimates  
487 owing to low concentrations of these elements in the clinopyroxene, close to  
488 the detection limit for analyses by LA-ICP-MS. These data are therefore not  
489 discussed further. Lithium is incompatible ( $D_{Li} = 0.1$ –0.4) in both Canary  
490 Islands and experimental clinopyroxene and, like Sr and Pb, becomes more  
491 compatible with increasing aegirine content in the clinopyroxene, plateauing  
492 at  $X_{Na}^{M2} = 0.4$  and decreasing thereafter (Figs. 7g, S6g). The actinides U  
493 and Th show contrasting partitioning behaviour; the former showing no cor-  
494 relation with aegirine content in the clinopyroxene, the latter becoming more  
495 incompatible with increasing aegirine content (Fig. 7h). The U and Th par-  
496 tition coefficients for our Canary Islands samples are similar to those for the  
497 Roman Province (Wood and Trigila, 2001; Fedele et al., 2009; Mollo et al.,  
498 2013, 2016), and are 1–2 orders of magnitude more incompatible relative to  
499 the experimental clinopyroxene.

500 *5.4. The effects of melt structure on element-partitioning*

501 The partitioning of trace-elements between crystals and melts is con-  
502 trolled by their relative activity in each phase and the exchange mechanisms  
503 by which their incorporation into crystals takes place (e.g., Jd-melt, Jd-DiHd  
504 and CaTS-DiHd exchanges have been shown to control REE incorporation  
505 in cpx, Putirka, 2008; Wood and Blundy, 2014; Mollo et al., 2017). As such,

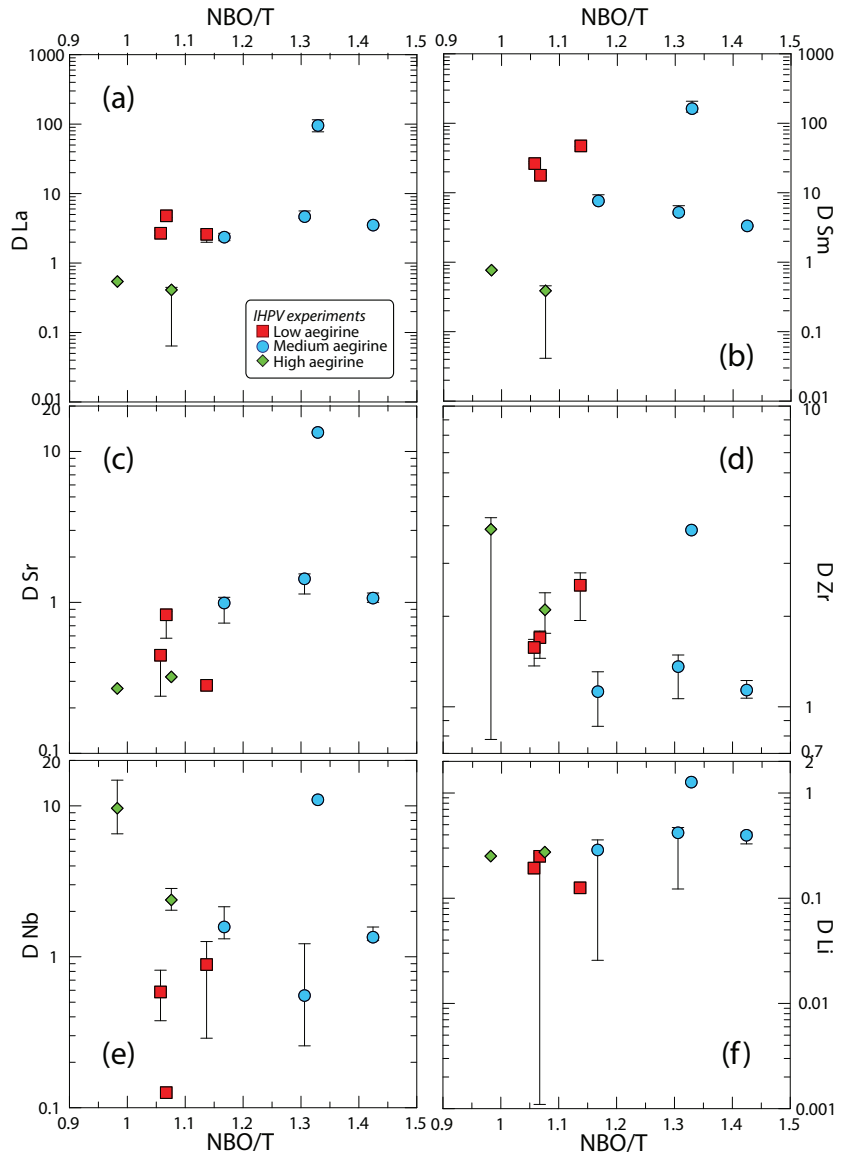


Figure 8: Diagrams of clinopyroxene–melt trace-element-partition coefficients for the IHPV experiments as a function of NBO/T of the quenched melt (Mysen et al., 1985). The water-saturated, sodic compositions investigated produce melts with highly depolymerised structures. The NBO/T ratio of these melts is not correlated with trace-element-partition coefficients, except weakly in the case of Sr. In highly polymerised systems ( $\text{NBO}/\text{T} < 0.49$ , Gaetani 2004) partition coefficients for REE and HFSE are negatively correlated with this parameter. (see Fig. 9 from Huang et al. 2006).

one might expect to see correlations between melt structural parameters and trace-element-partition coefficients. Such correlations have been reported by numerous authors (e.g., Schmidt et al., 2006; Mollo et al., 2017), but appear to be expressed over a limited range of melt compositions (Gaetani, 2004; Huang et al., 2006). A widely used descriptor for melt structure is the ratio of non-bonding oxygen anions to tetrahedrally-coordinated cations ( $\frac{NBO}{T}$ , Mysen et al., 1982, 1985). In relatively polymerised melts, where this ratio falls below 0.49, melt structure has been shown to have a significant influence on mineral–melt partition coefficients (Gaetani, 2004; Huang et al., 2006).

To calculate NBO/T for our experiments, we estimated melt Fe oxidation state from run temperatures and known  $fO_2$  buffer conditions (Kress and Carmichael, 1991). The recalculated total of major-element oxides (incl.  $Fe_2O_3$ ) was then used to approximate the water content of the quenched melts. Oxygen from this dissolved water was added into the NBO/T calculation, which followed Mysen et al. (1985). The high content of alkalies and dissolved water in the experiments presented here produced melts that have  $NBO/T = 0.98\text{--}1.42$ ; well above the compositional boundary reported by Gaetani (2004). Consistent with his findings, most trace-element-partition coefficients determined from our experiments are uncorrelated with the NBO/T ratio of the melt (Fig. 8). An exception is  $D_{Sr}$  that shows a weak positive correlation with NBO/T (Fig. 8c). NBO/T could not be calculate for our Canary Islands compositions because the water content of the melt prior to quench is not known.

Because partition coefficients between clinopyroxene and melt are controlled by the relative activity of elements in each of these two phases, an

531 empirical model to predict partition coefficients from both melt and mineral  
532 compositional terms has the highest potential for accuracy. Application of  
533 such a model would however require measurement of both mineral and melt  
534 phases, which would limit its geological utility. A similar model based only  
535 on clinopyroxene composition could be applied in a wider range of scenarios  
536 where melt composition cannot be directly measured, for example to cumu-  
537 late systems or to concentrically zoned phenocrysts. Because crystallisation  
538 is a thermodynamically controlled process, the composition of the melt and  
539 thus its effects on element-partitioning will, at least in part, be recorded by  
540 the composition of the clinopyroxene. This considered, we chose to calibrate  
541 a clinopyroxene-based empirical partitioning model, based on lattice-strain  
542 theory that would be applicable over a wide compositional range from tholei-  
543 itic basalts to peralkaline phonolites. Details are provided in the following  
544 sections.

545 *5.5. Fits to the lattice-strain model*

546 The equilibrium partitioning of trace-elements between minerals and melts  
547 is largely controlled by the structure of the crystal lattice, its elasticity (On-  
548 uma et al., 1968; Kumazawa, 1969; Weidner and Vaughan, 1982) and its  
549 ability to accommodate an excess or shortage in charge (Blundy et al., 1998;  
550 Wood and Blundy, 2001; Hanchar et al., 2001; Corgne and Wood, 2005). The  
551 lattice-strain model provides a framework in which the influence of these vari-  
552 ables on partitioning behaviour can be quantified, and thus predicted under  
553 conditions bracketed by a calibrating data set (Onuma et al., 1968; Blundy  
554 and Wood, 1994; Wood and Blundy, 2014). Lattice structure has a depen-  
555 dence on pressure, temperature and composition, and element-partitioning

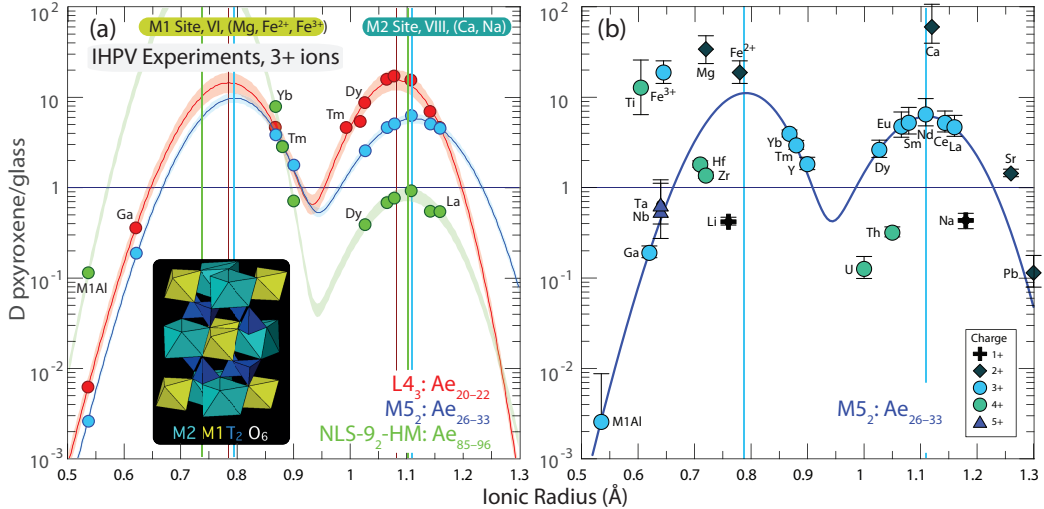


Figure 9: Non-linear weighted least-squares fits to element-partitioning data from the internally heated pressure vessel experiments following the lattice-strain model of Blundy and Wood (1994). (a) Representative fits to 3+ ion partitioning behaviour with examples for low (red), medium (blue) and high-aegirine (green) clinopyroxene experiments. (b) Measured partition coefficients for ions of 1+, 2+, 4+ and 5+ charges that are consistent with the lattice-strain model. Ionic radii are assigned to 6 or 8 fold co-ordination (Shannon, 1976), and were chosen to minimise residuals in the fit (cf. Olin and Wolff, 2010). Y was not included in the fitting routine for 3+ ions because of mass fractionation effects (ibid.). Vertical coloured lines indicate ideal ionic radii ( $r_0$ ) of M1 and M2 sites and shaded areas indicate 95% confidence intervals on the fits determined via bootstrapping. Uncertainties on the partition coefficients in (b) are  $1\sigma$ . Fitted lattice-strain parameters are given in Table 4.

is a thermodynamically-controlled process (e.g. Wood and Blundy, 1997).

Most trivalent ions, including the REE and Y enter the M2 site of clinopyroxene, which is typically 6- or 8-coordinated (Deer et al., 1992). Smaller trivalent ions, including Al, Cr, Ga, Sc, and in the case of Fe-rich clinopyrox-

560 ene the HREE may enter the smaller, octahedral M1 site (Olin and Wolff,  
 561 2010; Bédard, 2014). The high field-strength elements Ti, Zr, Hf, Nb and  
 562 Ta are typically hosted by the M1 site (Hill et al., 2000, 2011; Dygert et al.,  
 563 2014).

564 To investigate systematics in  $D_i$  values and the mechanisms by which  
 565 trace-elements are incorporated into clinopyroxene, element-partitioning be-  
 566 haviour was explored in light of the lattice-strain theory, quantitatively de-  
 567 scribed by the lattice-strain equation:

$$D_i^{mineral/melt} = D_0 \exp \left[ \frac{-4\pi E_s N_a}{RT} \left( \frac{r_0}{2} (r_0 - r_i)^2 - \frac{1}{3} (r_0 - r_i)^3 \right) \right] \quad (1)$$

568 where  $r_0$  is the ideal radius for the lattice site,  $E_s$  is the Young's modulus  
 569 (i.e., the lattice site stiffness),  $D_0$  is the strain-free partition coefficient,  $N_a$  is  
 570 Avagadro's number,  $R$  is the gas constant,  $T$  is temperature in Kelvin, and  
 571  $r_i$  is the ionic radius of the element in question, all radii in Å. We focused on  
 572 3+ ions that cover a wide range of radii and fitted lattice-strain parameters  
 573 for both the M1 and M2 sites of clinopyroxene (Fig. 9):

$$D_i^{cpx/melt} = D_0^{M2} \exp \left[ \frac{-4\pi E_s^{M2} N_a}{RT} \left( \frac{r_0^{M2}}{2} (r_0^{M2} - r_i)^2 - \frac{1}{3} (r_0^{M2} - r_i)^3 \right) \right] + D_0^{M1} \exp \left[ \frac{-4\pi E_s^{M1} N_a}{RT} \left( \frac{r_0^{M1}}{2} (r_0^{M1} - r_i)^2 - \frac{1}{3} (r_0^{M1} - r_i)^3 \right) \right] \quad (2)$$

574 Parabolae for 3+ ions were fitted for the M1 and M2 sites using the REE, Ga  
 575 and Al assigned to the M1 site of clinopyroxene (Fig. 9a). Fits are weighted  
 576 based on uncertainties for the element-partition coefficients. HREE have  
 577 higher element-partition coefficients than can predicted by substitution into

578 the M2 site, hence were fitted with ionic radii for sixfold coordination into  
579 the M1 site (*cf.* Olin and Wolff, 2010; Reguir et al., 2012). Lattice-strain  
580 parameters as obtained from fits to the data are shown in Table S1.

581 In some low-aegirine experiments and the Canary Islands rocks, lattice-  
582 strain fitting for 3+ ions at the M1 site was not possible, because too few  
583 HREE partitioned onto the M1 site of these clinopyroxene. Here, we chose  
584 to fit only lattice-strain parameters for the M2 site, or fix  $D_0^{3+}$  values for the  
585 M1 site to match those for the M2 site, and fit only the  $r_0$  and  $E_s$  parameters  
586 for the M1 site. Fitting of element-partitioning data for 1+, 2+ and 4+ ions  
587 was less successful owing to sparse coverage of suitable radii and detection-  
588 limit issues for some elements. Partition coefficients for 1+, 2+, and 4+  
589 elements follow radius- and charge-dependent trends consistent with lattice-  
590 strain theory and reported effects of charge on lattice-strain parameters (Fig.  
591 9b, e.g., Hazen and Finger, 1979; Law et al., 2000; Adam and Green, 2006).

592 *5.5.1. Effects of composition on ideal site size,  $r_0$*

593 As the composition of clinopyroxene shifts from augite toward aegirine,  
594 the size of the M1 and M2 sites, or strain-free radii ( $r_0$ ), should diverge fol-  
595 lowing the sizes of the major-element cations on these sites. Lattice-strain fits  
596 for 3+ cations indicate expansion of the M2 site between low and medium-  
597 aegirine clinopyroxene, with  $r_{0M2}^{3+}$  correlating well with Na replacing Ca (Figs.  
598 9, 10). Expansion of the M2 site stalls at  $r_{0M2}^{3+} \approx 1.12$  Å and  $X_{Na}^{M2} \approx 0.4$ ,  
599 changing little in size between medium and high-aegirine clinopyroxene. We  
600 suggest that this is a ‘saturation effect’, whereby the smaller ions in the T  
601 and M1 sites prevent further expansion of the M2 site as additional  $R_{M2}^{+}$   
602 is added to the clinopyroxene. For the M1 site of clinopyroxene, strain free

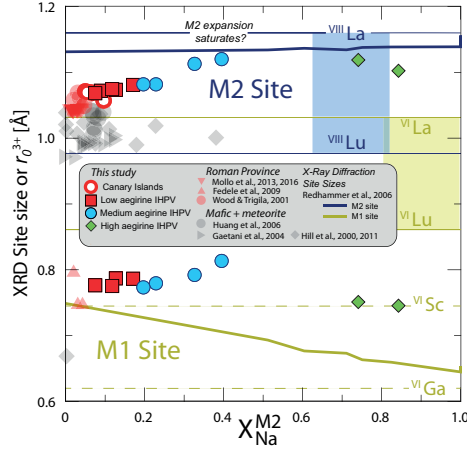


Figure 10: Diagram showing variation of ideal ionic radius  $r_0^{3+}$  with  $X_{\text{Na}}\text{M}_2$  for M1 and M2 sites of clinopyroxene. Shown for comparison are single crystal x-ray diffraction data from the hedenbergite-aegirine compositional join (heavy solid lines, from Redhammer et al., 2006). Shaded boxes represent the range of ionic radii for rare earth elements in VI and VIII coordination (Shannon, 1976). Literature data for the Roman Province, Italy are from Fedele et al. (2009); Mollo et al. (2013, 2016); Wood and Trigila (2001) and for mafic systems are from Hill et al. (2000, 2011); Gaetani (2004); Huang et al. (2006).

603 radii for  $R^{3+}$  cations indicate expansion between low and medium-aegirine  
 604 clinopyroxene and contraction between medium and high-aegirine clinopy-  
 605 roxene (Figs. 9, 10). These trends broadly follow the substitution of  $\text{Mg}^{2+}$   
 606 for  $\text{Fe}^{2+}$ , then  $\text{Fe}^{2+}$  for  $\text{Fe}^{3+}$  with increasing aegirine content in the clinopy-  
 607 roxene.

#### 608 5.5.2. The effect of cation charge on the $D_0$ parameter

609 The  $D_0$  parameter of the lattice-strain model describes ideal, strain-free  
 610 partitioning and tracks the solubility of an ideal cation in the mineral with  
 611 changing pressure, temperature and the bulk composition of the system

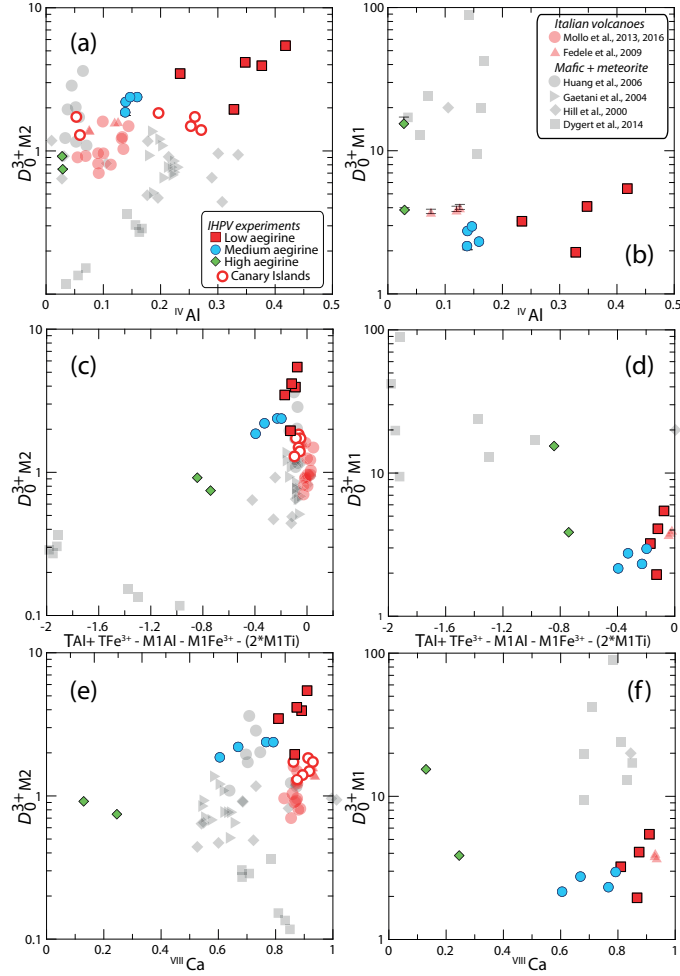


Figure 11: Strain-free partitioning coefficients ( $D_0$ ) for 3+ ions into clinopyroxene vs. various charge compensation mechanisms. (a,c,e) are for the M2 site, and (b,d,f) are for the M1 site. The diagrams show that variability in partitioning behaviour is highly dependent on mineral composition, and that variation between aegirine-rich clinopyroxene cannot be explained well by the same mechanisms as more mafic systems. Literature data for element-partitioning in Mafic + Meteorite and Roman Province compositions are from the compilation of Bédard (2014).  $1\sigma$  uncertainties are shown in (a, b) and are usually smaller than the symbol sizes.

(Wood and Blundy, 2014).  $D_0$  therefore correlates with the major-element composition of the clinopyroxene. Moreover, incorporation of trace-elements of a different charge introduces an electrostatic penalty that leads to a lower  $D_0$  for that charge (Wood and Blundy, 2001, 2003).

The average charge of major-elements on the M2 site of clinopyroxene decreases from 2+ to 1+ on the compositional join between Ca-rich diopside and Na-rich aegirine. Consequently, the electrostatic penalty for substituting a REE<sup>3+</sup> cation into the clinopyroxene M2 site is increased. Indeed,  $D_{0,M2}^{3+}$  decreases as Ca exchanges for Na (Fig. 11e). Conversely, as the average charge on the M1 site of clinopyroxene increases from 2+ toward 3+ in end-member aegirine, the electrostatic penalty incurred when substituting REE<sup>3+</sup> cations onto the M1 site is reduced (Fig. 11f). As a result,  $D_{0,M1}^{3+}$  increases by approximately an order of magnitude between our medium-aegirine and high-aegirine experimental clinopyroxene, an effect that when combined with the shrinking M1 site size, leads to strong fractionation of the HREE (Figs. 9 and 11f).

A positive correlation between Al<sup>T</sup> and partition coefficients for highly charged trace-elements has been extensively documented in studies on clinopyroxene (Lundstrom et al., 1994; Gaetani and Grove, 1995; Blundy et al., 1998; Francis and Minarik, 2008; Hill et al., 2011; Mollo et al., 2016). The low-aegirine experimental clinopyroxene and most of the Canary Islands rocks extend trends defined by clinopyroxene from mafic systems (Fig. 11a), whereas the remainder of the experimental data set and Canary Islands rocks show element-partitioning behaviour similar to the potassic Roman Province of Italy (Wood and Trigila, 2001; Fedele et al., 2009; Mollo et al., 2016), con-

637 firming that an Al<sup>T</sup>-controlled substitution mechanism extends to peralkaline  
638 conditions (Figs. 7, 11a).

639 Tetrahedral Al is thought to facilitate incorporation of REE<sup>3+</sup> cations  
640 onto the M2 site of clinopyroxene by replacing Si<sup>4+</sup>, thereby reducing local  
641 charge and thus the electrostatic penalty associated with incorporation of  
642 REE (Blundy et al., 1998). The substitution of Fe<sup>3+</sup> for tetrahedral Si<sup>4+</sup> can  
643 be expected to have a similar effect. Conversely, R<sup>3+</sup> ions on the neighbouring  
644 M1 site should hinder incorporation of REE on the M2 site, because they  
645 increase local charge by replacing R<sup>2+</sup> ions, such as Mg<sup>2+</sup> and Fe<sup>2+</sup>. This  
646 electrostatic penalty should apply doubly to Ti<sup>4+</sup> on the M1 site. This effect  
647 is consistent with our experimental data (Fig. 11c), but is not obvious in the  
648 natural samples, nor in the majority of the literature experimental data. It  
649 would thus appear that other factors, such as melt structure, have a stronger  
650 control on  $D_{REE}$  (e.g. Prowatke and Klemme, 2005).

651  $D_0^{3+}$  parameters for the M1 site are strongly correlated with those for the  
652 M2 site, except at aegirine concentrations exceeding 50 mol.%. Similarities to  
653 M2 partitioning behaviour likely reflect the dominance of T-site substitution  
654 mechanisms in augite clinopyroxene. In the high-aegirine clinopyroxene, T-  
655 site substitutions become less important as the T-sites become saturated with  
656 Si<sup>4+</sup> (Fig. 5). The replacement of Fe<sup>3+</sup> at the M1 site by 3+ trace-elements  
657 does introduce a charge penalty, therefore  $D_{0M1}^{3+}$  increases accordingly.

658 *5.6. An element-partitioning model extending to aegirine clinopyroxene*

659 Element partition coefficients vary systematically with the physiochemi-  
660 cal conditions of natural and synthetic magmas (cf. Wood and Blundy, 2003).  
661 Consequently, a host of models have been presented to describe the system-

662 atics of element-partitioning between clinopyroxene and silicate melts (Wood  
663 and Blundy, 1997, 2001; Hill et al., 2011; Yao et al., 2012; Sun and Liang,  
664 2012; Bédard, 2014; Dygert et al., 2014; Mollo et al., 2016). The majority of  
665 these models are based on lattice-strain theory and predict how the lattice  
666 parameters  $r_0$ ,  $E_s$ , and  $D_0$  vary with composition, temperature and pressure.  
667 This semi-thermodynamic approach theoretically permits calculation of par-  
668 tition coefficients for any trace-element, at any set of  $P - T - X$  conditions.  
669 In reality, all models have a limited working range, as restricted by the input  
670 data set. Because existing partitioning models do not reproduce the high  
671  $r_{0,M2}^{3+}$  values for clinopyroxene with aegirine contents  $\geq 50$  mol % (Fig. 12a),  
672 they cannot accurately predict REE partitioning behaviour for strongly per-  
673 alkaline systems. Here, we present a new empirical model that is calibrated  
674 on both our experimental work and natural partition coefficients from Ca-  
675 nary Islands rocks, as well as existing partitioning data from the literature  
676 (compilation of Bédard, 2014, Fig. 12, Table S1).

677 Our model focuses on the dependence of element-partitioning on clinopy-  
678 roxene composition, temperature and pressure only. While partition coeffi-  
679 cients are thermodynamically controlled by activity of elements in both the  
680 crystal and the melt phase (Wood and Blundy, 2014), and while melt struc-  
681 ture has been shown to influence element-partitioning (Huang et al., 2006;  
682 Schmidt et al., 2006; Mollo et al., 2017), it is not always possible to measure  
683 melt composition directly. For example, equilibrium melt compositions can-  
684 not be measured for the cores of zoned clinopyroxene phenocrysts in tephra,  
685 or indeed for any crystal from an intrusion in which gravitational segrega-  
686 tion of phases has occurred. Therefore, while the predictive power of a model

687 based only on the compositions of the crystal should be lower than that of  
688 a model based on both crystal and melt compositions, a crystal-only model  
689 may be applied to a wider spectrum of geological scenarios. Melt composi-  
690 tion should, at least in part, be recorded by the major-element composition  
691 of the clinopyroxene.

692 *5.6.1. The clinopyroxene M2 site*

693 To find the principal physiochemical factors that affect element-partitioning  
694 at the M2 site of clinopyroxene, a stepwise least-squares multiple linear re-  
695 gression analysis was performed using the lattice-strain parameters  $r_0^{3+}$ ,  $E_s^{3+}$   
696 and  $D_0^{3+}$ , temperature, pressure and clinopyroxene composition as inputs.  
697 Input parameters were initially examined in binary scatter diagrams to as-  
698 certain whether correlations with lattice-strain parameters were linear. If  
699 not, interaction compositional terms were added to the initial set of possible  
700 fitting parameters that had linear correlations with lattice-strain parameters  
701 (e.g.  $X_{Al+Fe^{3+}}^T$ ). Intensive variables for multiple regression models for  $r_0$ ,  
702  $E_s$  and  $D_0$  were introduced following a hierarchical forward selection crite-  
703 rion with switching. The largest number of significant terms to describe a  
704 lattice-strain parameter was eight for  $E^{M2}$  (c.95%, cf. Supplement S4).

705 Because of systematic covariation of compositional parameters in our  
706 small data set of experiments and natural samples ( $n = 16$ ), a model cal-  
707 ibrated with these points alone would be unable to deconvolve the effects  
708 of each major-element on partitioning behaviour. We have therefore added  
709 published experiments and natural phenocryst-glass pairs ( $n = 75$ ) to assem-  
710 ble a database covering a wide range of composition, pressure, temperature  
711 and oxygen fugacity (data from compilation of Bédard 2014, and Mollo et al.

712 2016, 0.0001–3.5 GPa, 650–1345 °C,  $\log f\text{O}_2 = \text{IW}$  to MH  $\approx \Delta\text{QFM}$  -5  
 713 to +5). clinopyroxene compositions cover  $X\text{Mg}$  0.031–1,  $X_{\text{Na}}^{M2}$  0–0.84 and  
 714  $\text{Al}^T$  0–0.49 c.f.u. and melt compositions vary widely in terms of Mg# (0–  
 715 100) and  $X\text{H}_2\text{O}$  (0–0.38). REE partition coefficients also vary significantly  
 716 (e.g.  $D_{\text{La}}$  0.01–4.79;  $D_{\text{Sm}}$  0.02–47.24, and  $D_{\text{Yb}}$  0.11–8.00). The majority  
 717 of partition coefficients in the training data set were measured via SIMS  
 718 or LA-ICP-MS, minimising analytical uncertainty (e.g. from analyses by  
 719 electron-microprobe).

720 The resultant empirical model accounts well for changes in lattice-strain  
 721 parameters over a range of compositions from basalt to peralkaline phono-  
 722 lite, faithfully reproducing large  $r_0^{M2}$  values typical for sodic clinopyroxene  
 723 (Fig. 12, model coefficients in Table 5). Student t-tests show that all of the  
 724 independent variables included in the models are significant at the 95% con-  
 725 fidence level and PRESS  $R^2$  values were obtained by repeatedby randomly  
 726 subsampling the dataset (Stevens, 1996), are close to  $R^2$  values calculated by  
 727 regular methods, indicating robust models with high predictive power. Full  
 728 multiple regression reports are available in Supplement S4. Equations gen-  
 729 erated by the multiple linear regression calculations are given below for the  
 730 M2 site, where  $a_i$  are the regression coefficients for the respective variables:  
 731

$$\ln D_0^{M2} = a_1 + a_2 T + a_3 X_{\text{Al}+\text{Fe}^{3+}}^T + a_4 X_{\text{Ti}}^{M1} + a_5 X_{\text{Al}-\text{Fe}^{3+}}^{M1} + a_6 X_{\text{Fe}^{2+}}^{M2} \quad (3)$$

$$E^{M2} = a_7 + a_8 P + a_9 X_{Al+Fe^{3+}}^T + a_{10} X_{Al}^{M1} + a_{11} X_{Mg}^{M1} + a_{12} X_{Ti}^{M1} + a_{13} X_{Mg}^{M2} + a_{14} X_{Mg} \quad (4)$$

$$r_0^{M2} = a_{15} + a_{16} T + a_{17} X_{Al-Fe^{3+}}^{M1} + a_{18} X_{Ti}^{M1} + a_{19} X_{Ca}^{M2} + a_{20} X_{Na}^{M2} \quad (5)$$

732 The model for  $r_0^{M2}$  is robust with high predictive power and incorporates  
 733 compositional controls from the M1 and M2 sites, as well as temperature.  
 734 Elevated concentrations of large M2 cations  $\text{Ca}^{2+}$  and  $\text{Na}^+$  are correlated  
 735 with large M2 sites.  $\text{Ti}^{4+}$  cations in the neighbouring M1 site are also cor-  
 736 related with expansion of the M2 site, and the concentration of small  $\text{Al}^{3+}$   
 737 minus larger  $\text{Fe}^{3+}$  on the M1 site is negatively correlated with  $r_0^{M2}$ . The neg-  
 738 ative correlation between  $r_0^{M2}$  and temperature reflects the sum of changes  
 739 to major-element composition that lead to smaller clinopyroxene M2 sites at  
 740 higher temperatures. This compositional effect swamps the minor influence  
 741 of thermal expansion.

742  $D_0^{M2}$  is reasonably well predicted and incorporates compositional terms  
 743 from all three sites in clinopyroxene and temperature. The positive effect  
 744 of tetrahedral  $\text{R}^{3+}$  on  $D_0^{M2}$  is the largest contribution to the model, which  
 745 is consistent with published studies (see above). The relationship between  
 746 clinopyroxene compositional terms on the M1 and M2 sites and  $D_0$  are in-  
 747 direct and are tied to the solubility of the mineral in the melt (Wood and  
 748 Blundy, 2003), which in turn is tied to the physiochemical conditions of the  
 749 system (largely melt composition). The model for  $D_0^{M2}$  is less robust than  
 750 that for  $r_0^{M2}$ , largely because there are melt compositional effects that are

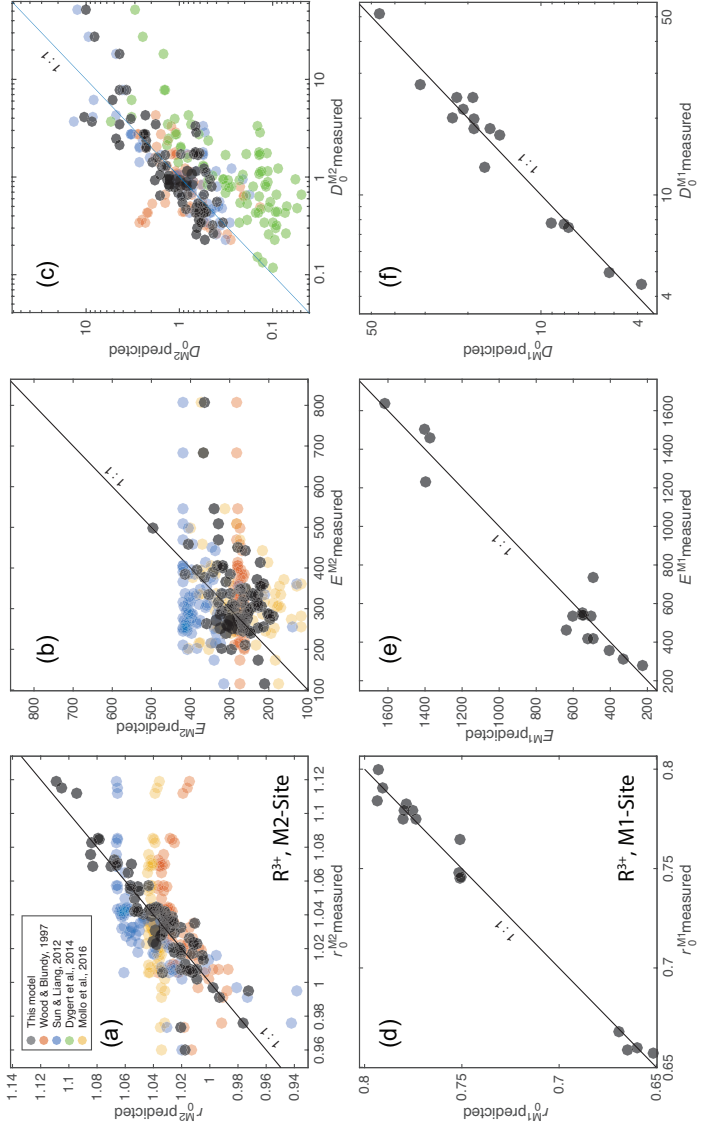


Figure 12: Measured vs. predicted model values for lattice-strain parameters for the M2 and M1 sites of clinopyroxene. The new models presented here were generated via a stepwise multiple linear regression procedure following a hierarchical forward selection criterion with switching. Full regression reports are in Supplement S4 and model equations are in the main text.

751 not recorded in the composition of the clinopyroxene. We tested the Mg#  
752 and  $X\text{H}_2\text{O}$  of the melt, neither of which are significant predictors for  $D_0^{M^2}$ .

753 The model for  $E^{M^2}$  is less well-constrained than for the other two M2  
754 lattice-strain parameters, suggesting that M2 site stiffness is not tied strongly  
755 to clinopyroxene composition, temperature or pressure. Despite a signifi-  
756 cantly lower predictive power, this model still has physical grounding. Stiff-  
757 ness of the M2 site is positively correlated with pressure, as might be expected  
758 following a simple Hooke's law relationship, and there are some subtle com-  
759 positional controls imparted by the T and M1 sites. The poor correlation  
760 between  $E^{M^2}$ , clinopyroxene composition, temperature and pressure is also  
761 evident in published element-partitioning models, where  $E^{M^2}$  is either poorly  
762 predicted (Fig. 12b), or set to a fixed value (e.g. Dygert et al., 2014).

763 Diagrams of measured vs. predicted D values for  $\text{R}^{3+}$  cations are given in  
764 Figure 13a, showing the predictive power of the models over a compositional  
765 range between basalt and peralkaline phonolite. For the M2 site, 95% of  
766 the measured  $\text{R}^{3+}$  partition coefficients are reproduced within a factor of  
767  $\frac{+2.5}{-2.9}$  (hard dashed lines), and in extreme cases, the model still reproduces D  
768 values within an order of magnitude, sufficient for the prediction of element-  
769 partitioning trends over a wide range of  $P - T - X$ .  $D_{MREE}$ , such as Sm,  
770 are reproduced more faithfully than  $D_{LREE}$ , because their radius is closer to  
771  $r_0^{M^2}$  (Fig. 13c,d), and therefore prediction of their partitioning behaviour is  
772 affected less strongly by inaccuracies in predicted  $E^{M^2}$  values.

773 *5.6.2. The clinopyroxene M1 site*

774 Using a methodology similar to the M2 site, we fitted a predictive model  
775 for partitioning of  $\text{R}^{3+}$  cations onto the smaller, 6-coordinated M1 site of

776 clinopyroxene. Lattice-strain parabola were constrained by partitioning data  
 777 for Cr, Ga, Sc, and where suitable, the HREE Tm, Yb and Lu (Our IHPV  
 778 experiments plus Hill et al. 2000; Fedele et al. 2009; Mollo et al. 2013; Dygert  
 779 et al. 2014). The training data set for the M1 site partitioning model is  
 780 small relative to that for the M2 site ( $n = 18$ ), and because it is strongly  
 781 skewed toward alkaline compositions, it has lower predictive power and is  
 782 not recommended for application to mafic magmatic systems. Equations for  
 783 the M1 site lattice-strain parameters, as generated by multiple linear least  
 784 squares regression, are given below and shown in Figure 12 where  $b_i$  are the  
 785 regression coefficients (Table 5) for the respective variables:

$$\ln D_0^{M1} = b_1 + b_2 X_{Al}^T + b_3 X_{Fe^{2+}}^{M1} + b_4 X_{Ca}^{M2} + b_5 X_{Na}^{M2} \quad (6)$$

$$E^{M1} = b_6 + b_7 T + b_8 P + b_9 X_{Mg}^{M1} \quad (7)$$

$$r_0^{M1} = b_{10} + b_{11} P + b_{12} X_{Mg}^{M2} + b_{13} X_{Fe^{3+}}^{M1} + b_{14} X_{Ca}^{M2} \quad (8)$$

786 The model for  $r_0^{M1}$  is robust and accurately reproduces the input data  
 787 set. A negative pressure term may reflect compressional strain on the crystal  
 788 lattice. Large  $Fe^{3+}$  cations have a positive effect on the size of the M1 site,  
 789 while smaller  $Mg^{2+}$  cations on the neighbouring M2 site have a negative effect  
 790 on M1 site size. The small negative  $X_{Ca}^{M2}$  term is indirectly related to the  
 791 size of the M1 site.

792         $E^{M1}$  is predicted more accurately than  $E^{M2}$  and is largely described by  
793 variations in temperature and pressure. Much like the M2 site, stiffness of  
794 the M1 site appears to be controlled dominantly by physicochemical factors  
795 that are not recorded in the composition of the clinopyroxene.

796        The model for  $D_0^{M1}$  contains compositional terms from all three crystal-  
797 lographic sites in clinopyroxene.  $X_{Al}^T$  has a strong positive correlation with  
798  $D_0^{M1}$ , consistent with a charge compensation mechanism that aids incorpora-  
799 tion of R<sup>3+</sup> cations, while terms for M1 and M2 site cations may be indirectly  
800 recording melt compositional effects. Because  $D_0^{M1}$  is unusually high for our  
801 high-aegirine experiments, they had to be excluded from the fitting procedure  
802 to permit model convergence. The models for  $r_0^{M1}$  and  $E^{M1}$  are calibrated  
803 for use all the way to end-member aegirine, but this was not possible for the  
804  $D_0^{M1}$  term, which is calibrated for use up to  $\sim\text{Ae}_{50}$ . Further experiments  
805 at conditions between those that generated our medium and high-aegirine  
806 clinopyroxene would be required to better constrain the clinopyroxene com-  
807 positional record of  $D_0^{M1}$  in strongly peralkaline Fe-rich magmas.

808        When applied to our experimental data, and the compilation of partition  
809 coefficients from the Roman Province (Fedele et al., 2009; Mollo et al., 2013,  
810 2016), the M1 stepwise model reproduces element-partitioning data to a fac-  
811 tor of  $\frac{+7}{-11}$  at the 95% confidence interval (Fig. 13b). Full regression reports  
812 are provided in Supplement S4.

813        For convenience, we provide an EXCEL spreadsheet for calculation of  
814 clinopyroxene-melt element-partition coefficients for any trace-element of 3+  
815 valence that is large enough to fit onto the M1 or M2 sites of clinopyroxene  
816 (Supplement S5). To assess the utility of the partitioning models and to

monitor for potential introduction of radius-dependent bias, we show predicted REE patterns normalised to measured ratios for some literature data and our internally heated pressure vessel experiments (Fig. 14). The model accurately reproduces REE patterns at all compositions, except for HREE on the M1 site of clinopyroxene at aegirine contents exceeding ~50 mol% (NLS experiments).

### 5.7. Implications for formation of REE deposits in evolved alkaline intrusions

The solubility of REE and HFSE minerals is strongly enhanced in peralkaline melts (Watson, 1979; Linnen and Keppler, 1997; Boehnke et al., 2013; Aseri et al., 2015), thus the high concentration of these elements in peralkaline systems may (partially) reflect this fact (Dostal, 2017). Melts containing high concentrations of REE and HFSE are thought to be generated through low degrees of partial melting in the source, followed by residual enrichment during protracted fractional crystallisation (Marks and Markl, 2017). The budget of REE and HFSE in a fractionating magma is influenced by the mineralogy of the crystallising assemblage, and the extent to which these elements are incorporated at minor or trace concentrations.

Clinopyroxene is a major ferromagnesian phase that is commonly saturated throughout the entire differentiation histories of peralkaline magmatic systems (Ablay et al., 1998; Marks and Markl, 2001; Möller and Williams-Jones, 2016). The composition of the fractionating clinopyroxene has a major impact on the absolute REE concentrations and REE pattern of the residual melt, and ultimately on the ability of a system to develop economic concentrations of the REE (Fig. 15, e.g. Kogarko, 1990; Sørensen, 1992; Marks et al., 2011). Clinopyroxene in alkaline magmatic systems is initially cal-

cic for mafic melts, and becomes increasingly sodic as crystal fractionation proceeds (Marks et al., 2004). Although the REE are compatible in the majority of our experimentally generated clinopyroxene, those approaching aegirine end-member composition, as found in evolved alkaline magmatic systems have the lowest  $D_{REE}$  values (Fig. 6). Strongly alkaline magmatic systems are thought to crystallise abundant Ca-pyroxene early in their evolution which may deplete residual liquids with respect to REEs. Consequently, even though crystallisation of Na-pyroxene could enrich residual liquids with REE, the resultant concentration of these metals in the melt would remain low. However, clinopyroxene is not the only phase to crystallise from alkaline magmas, and the majority of additional silicate phases, such as olivine, biotite and feldspar have  $D_{REE} << 1$ , typically 1-4 orders of magnitude lower than clinopyroxene (Larsen, 1979; Kovalenko et al., 1988; Mahood and Stimmel, 1990; Fedele et al., 2015). Consequently, if the mode of clinopyroxene is low enough, the bulk  $D_{REE}$  of the crystallising assemblage would remain below unity, allowing the REE to become enriched in the residual silicate melt.

To give insight into the optimum conditions for residual magmatic enrichment of the REE in alkaline systems we modelled the evolution of REE concentrations in the melt during fractional crystallisation of a nepheline syenite body (Fig. 15). Phase relation data and clinopyroxene compositions are from the experimental study of Giehl et al. (2013). Their starting composition, based on the MiKa dyke, from the Gardar Province, Greenland, is already extremely evolved, with  $Mg\# = 2$ ,  $(Na + K)/Al = 1.44$  and  $FeO^* = 12$  wt.%.

867 In these models, crystallisation under water-bearing, oxidising conditions  
868 produces a high fraction of clinopyroxene that depletes residual melts with  
869 respect to Sm, while subtly enriching La. Dry conditions promote abun-  
870 dant alkali feldspar (Afs) crystallisation, which effectively enriches the REE  
871 content of residual melts. Under oxidising, dry conditions, the La/Sm ra-  
872 tio of the residual melt increases with fractionation, because Sm is more  
873 effectively incorporated into clinopyroxene. Residual enrichment is most ef-  
874 fective under dry, reducing conditions because of a relatively lower fraction  
875 of clinopyroxene within the crystallising assemblage. Because of this, the  
876 REE enrichment path of the residual melt is close to that of ideal Rayleigh  
877 fractionation. Under these reducing, dry conditions and at a temperature of  
878 750°C, the experiments of Giehl et al. (2013) attained a crystal fraction of  
879 0.8. Here, residual melts would have and 3.2 times La concentration and 2  
880 times the Sm concentration relative to their starting composition.

881 Considering these mechanisms, alongside our experimental and Canary  
882 Islands data, the best systems to develop high REE concentrations are those  
883 that would produce small proportions of Ca-pyroxene early in their crystalli-  
884 sation histories, quickly evolving to more sodic compositions that crystallise  
885 aegirine clinopyroxene. Cooling under low-pressure, dry, reducing conditions  
886 produces abundant alkali feldspar that in the case of a peralkaline compo-  
887 sition, would serve to further increase the alkalinity of the residual melt.  
888 Low degrees of source melting would produce primary melts with (1) high  
889 REE concentrations and (2) low melt Mg + Fe, and low modal abundance  
890 of clinopyroxene, which would aid enrichment in residual melts via fractional  
891 crystallisation.

892        The HREE-rich nature of peralkaline magmatic systems, both granites  
893        and nepheline syenites, is compatible with fractionation of moderately sodic  
894        clinopyroxene that have high  $D_{LREE}/D_{HREE}$  (e.g. Möller and Williams-  
895        Jones, 2016; Dostal, 2017). As crystal fractionation progresses and clinopy-  
896        roxene compositions evolve toward the aegirine end-member composition,  
897         $D_{LREE}/D_{HREE}$  decreases (Fig. 6). This systematic change in element-  
898        partitioning behaviour would result in strong HREE enrichment in aegirine-  
899        pyroxene cumulates, and would enrich the residual melt with respect to  
900        LREE-MREE.

901        **Conclusions**

- 902        • Our experiments reveal three distinct element-partitioning behaviours  
903        for Na-rich clinopyroxene that depend on aegirine content. Each of  
904        these is associated with a distinct major-element exchange vector. We  
905        do not have the compositional resolution to know if the transition be-  
906        tween these behaviours is smooth or step-like.
- 907        • Fits to the lattice-strain model of Blundy and Wood (1994) indicate  
908        expansion of the M2 site with increasing  $\text{Na}_{\text{M}2}^{+}$ , to a maximum  $r_{0,\text{M}2}^{3+}$  of  
909        1.12 Å at  $\text{Na}_{\text{M}2}^{+} = 0.4$  c.f.u. Further expansion did not occur at higher  
910        Na contents.
- 911        • Both the M1 and M2 sites shrink at high-aegirine contents in response  
912        to increasing  $\sum \text{R}_{\text{M}1}^{3+}$ .
- 913        • Charge effects lead to a progressive increase in  $D_0^{\text{M}1}$  at the expense  
914        of  $D_0^{\text{M}2}$ , as the exchanges  $\text{Ca}^{2+}$  for  $\text{Na}^{+}$  and  $\text{M}^{2+}$  for  $\text{Fe}^{3+}$  take place.

915 Much like in systems of lower alkalinity, REE incorporation into clinopy-  
916 roxene is dominated by coupled Al–Si substitutions at the T-site.

- 917 • Existing predictive models for clinopyroxene/melt element-partitioning  
918 do not accurately reproduce the large M2 site ( $r_{0,M2}^{3+}$ ) of clinopyroxene  
919 with aegirine content exceeding 50 mol%. We have calibrated a new  
920 empirical model that may be applied to any composition between basalt  
921 and peralkaline phonolite, based on our data from experiments and  
922 natural systems, as well as a large compilation of partition coefficients  
923 from the literature.
- 924 • Crystallisation of abundant Ca-Mg rich clinopyroxene depletes the resid-  
925 ual melts of REE, and inhibits or terminates magmatic enrichment  
926 processes.
- 927 • Element partitioning systematics suggest that nepheline syenites which  
928 host REE deposits must originate from low-degree melts with sufficient  
929 alkali enrichment to saturate clinopyroxene similar to our medium-  
930 aegirine clinopyroxene ( $Ae_{25--50}$ ). Fractionation of such clinopyroxene  
931 enriches residual melts with respect to the HREE, in accord with the  
932 composition of REE-mineralised nepheline syenite systems.

933 **Acknowledgements**

934 We thank the Geo.X partners GFZ and Universität Potsdam for access to  
935 the HP-GeoMatS Lab, Don Baker for assistance with preparation of starting  
936 materials, Bruce Watson and Volker Möller for providing samples of Mud  
937 Tank zircon and the Nechalacho rocks, respectively, Hans Peter Nabein,

938 Maria Stuff and Julia Pohlenz for assistance with HP experimental equip-  
939 ment, Toby Soutar for help with preparation of the Canary Islands samples,  
940 Lang Shi and Glenn Poirier for assistance with electron-microprobe analyses,  
941 and Anna Jung for assistance with laser ICP-MS analyses. The manuscript  
942 benefited from discussions with Longbo Yang, Rebecca Paisley, Shane Rooy-  
943 akkers and Jean Bédard. Silvio Mollo, Lorenzo Fedele and an anonymous  
944 reviewer are thanked for their insightful feedback. Nelson Eby is thanked for  
945 editorial handling. This work was funded by PhD scholarships to C.B. from  
946 Geotop, DIVEX, and the SEG Canada Foundation, and operating grants to  
947 V.vH. and J.S. from the Natural Sciences and Engineering Research Coun-  
948 cil of Canada (grant numbers RGPIN-2014-05955, RGPAS-462335-2014) and  
949 the FQRNT team research project program.

950 **References**

- 951 Ablay, G.J., Carroll, M.R., Palmer, M.R., Martí, J., Sparks, R.S.J.,  
952 1998. Basanite–phonolite lineages of the Teide–Pico Viejo volcanic  
953 complex, Tenerife, Canary Islands. *Journal of Petrology* 39, 905–936.  
954 doi:10.1093/petroj/39.5.905.
- 955 Ablay, G.J., Ernst, G.G.J., Marti, J., Sparks, R.S.J., 1995. The 2 ka sub-  
956 plinian eruption of Montaña Blanca, Tenerife. *Bulletin of Volcanology* 57,  
957 337–355. doi:10.1007/BF00301292.
- 958 Adam, J., Green, T., 2006. Trace element partitioning between mica- and  
959 amphibole-bearing garnet lherzolite and hydrous basanitic melt: 1. Exper-  
960 imental results and the investigation of controls on partitioning behaviour.

- 961 Contributions to Mineralogy and Petrology 152, 1–17. doi:10.1007/s00410-  
962 006-0085-4.
- 963 Akasaka, M., Onuma, K., 1980. The join CaMgSi<sub>2</sub>O<sub>6</sub>-CaFeAlSiO<sub>6</sub>-  
964 CaTiAl<sub>2</sub>O<sub>6</sub> and its bearing on the Ti-rich fassaitic pyroxenes. Contributions  
965 to Mineralogy and Petrology 71, 301–312. doi:10.1007/BF00371672.
- 966 Albert, H., Costa, F., Martí, J., 2015. Timing of magmatic processes and  
967 unrest associated with mafic historical monogenetic eruptions in Tenerife  
968 Island. Journal of Petrology 56, 1945–1966. doi:10.1093/petrology/egv058.
- 969 Andújar, J., Scaillet, B., 2012. Experimental constraints on parameters con-  
970 trolling the difference in the eruptive dynamics of phonolitic magmas: the  
971 case of Tenerife (Canary Islands). Journal of Petrology 53, 1777–1806.  
972 doi:10.1093/petrology/egs033.
- 973 Aseri, A.A., Linnen, R.L., Che, X.D., Thibault, Y., Holtz, F., 2015. Effects of  
974 fluorine on the solubilities of Nb, Ta, Zr and Hf minerals in highly fluxed  
975 water-saturated haplogranitic melts. Ore Geology Reviews 64, 736–746.  
976 doi:10.1016/j.oregeorev.2014.02.014.
- 977 Beard, C.D., 2018. Mineral-melt trace element partitioning in alkaline mag-  
978 matic systems. Phd thesis. McGill University, Montreal, Canada.
- 979 Bédard, J.H., 2014. Parameterizations of calcic clinopyroxene - Melt trace  
980 element partition coefficients. Geochemistry, Geophysics, Geosystems 15,  
981 303–336. doi:10.1002/2013GC005112.
- 982 Behrens, H., Hahn, M., 2009. Trace element diffusion and viscous flow in

- 983 potassium-rich trachytic and phonolitic melts. *Chemical Geology* 259, 63–  
984 77. doi:10.1016/j.chemgeo.2008.10.014.
- 985 Berndt, J., Liebske, C., Holtz, F., Freise, M., Nowak, M., Ziegenbein,  
986 D., Hurkuck, W., Koepke, J., 2002. A combined rapid-quench and H<sub>2</sub>-  
987 membrane setup for internally heated pressure vessels: description and  
988 application for water solubility in basaltic melts. *American Mineralogist*  
989 87, 1717–1726. doi:10.1029/JB089iB10p08540.
- 990 Blundy, J., Wood, B., 1994. Prediction of crystal–melt partition coefficients  
991 from elastic moduli. *Nature* 372, 452–454. doi:10.1038/372452a0.
- 992 Blundy, J.D., Robinson, J.A.C., Wood, B.J., 1998. Heavy REE are compat-  
993 able in clinopyroxene on the spinel lherzolite solidus. *Earth and Planetary  
994 Science Letters* 160, 493–504. doi:10.1016/S0012-821X(98)00106-X.
- 995 Bohnke, P., Watson, E.B., Trail, D., Harrison, T.M., Schmitt, A.K.,  
996 2013. Zircon saturation re-revisited. *Chemical Geology* 351, 324–334.  
997 doi:10.1016/j.chemgeo.2013.05.028.
- 998 Borchert, M., Wilke, M., Schmidt, C., Cauzid, J., Tucoulou, R., 2010. Par-  
999 titioning of Ba, La, Yb and Y between haplogranitic melts and aque-  
1000 ous solutions: An experimental study. *Chemical Geology* 276, 225–240.  
1001 doi:10.1016/j.chemgeo.2010.06.009.
- 1002 Boudreau, A.E., 2004. PALLADIUM, a program to model the chromato-  
1003 graphic separation of the platinum-group elements, base metals and sulfur  
1004 in a solidifying pile of igneous crystals. *Canadian Mineralogist* 42, 393–403.  
1005 doi:10.2113/gscanmin.42.2.393.

- 1006 Brown, R.J., Barry, T.L., Branney, M.J., Pringle, M.S., Bryan, S.E., 2003.  
1007 The Quaternary pyroclastic succession of southeast Tenerife, Canary Is-  
1008 lands: explosive eruptions, related caldera subsidence, and sector collapse.  
1009 Geological Magazine 140, 265–288. doi:10.1017/S0016756802007252.
- 1010 Bryan, S.E., Martí, J., Cas, R.A.F., 1998. Stratigraphy of the Bandas del  
1011 Sur Formation: an extracaldera record of Quaternary phonolitic explo-  
1012 sive eruptions from the Las Cañadas edifice, Tenerife (Canary Islands).  
1013 Geological Magazine 135, 605–636. doi:null.
- 1014 Carracedo, J.C., Badiola, E.R., Guillou, H., Paterne, M., Scaillet, S.,  
1015 Torrado, F.J.P., Paris, R., Fra-Paleo, U., Hansen, A., 2007. Eruptive  
1016 and structural history of Teide Volcano and rift zones of Tenerife, Ca-  
1017 nary Islands. Geological Society of America Bulletin 119, 1027–1051.  
1018 doi:10.1130/B26087.1.
- 1019 Carroll, M.R., Blank, J.G., 1997. The solubility of H<sub>2</sub>O in phonolitic melts.  
1020 American Mineralogist 82, 549–556. doi:10.1093/petrology/32.5.1021.
- 1021 Chou, I.M., 1986. Permeability of precious metals to hydrogen at 2 kb total  
1022 pressure and elevated temperatures. American Journal of Science 286,  
1023 638–658.
- 1024 Corgne, A., Wood, B.J., 2005. Trace element partitioning and substitu-  
1025 tion mechanisms in calcium perovskites. Contributions to Mineralogy and  
1026 Petrology 149, 85–97. doi:10.1007/s00410-004-0638-3.
- 1027 Costa, F., Chakraborty, S., Dohmen, R., 2003. Diffusion coupling between  
1028 major and trace elements and a model for the calculation of magma cham-

- ber residence times using plagioclase. *Geochimica et Cosmochimica Acta* 67, 2189–2200. doi:10.1016/S0016-7037(00)01345-5.
- Coumans, J.P., Stix, J., Clague, D.A., Minarik, W.G., Layne, G.D., 2016. Melt-rock interaction near the Moho: Evidence from crystal cargo in lavas from near-ridge seamounts. *Geochimica et Cosmochimica Acta* 191, 139–164. doi:10.1016/j.gca.2016.07.017.
- Deer, W.A., Howie, R.A., Zussman, J., 1992. An introduction to the rock-forming minerals. Longman Group Ltd, New York.
- Dostal, J., 2017. Rare earth element deposits of alkaline igneous rocks. *Resources* 6, 1–12. doi:10.3390/resources6030034.
- Downes, H., Balaganskaya, E., Beard, A., Liferovich, R., Demaiffe, D., 2005. Petrogenetic processes in the ultramafic, alkaline and carbonatitic magmatism in the Kola Alkaline Province: A review. *Lithos* 85, 48–75. doi:10.1016/j.lithos.2005.03.020.
- Droop, G.T.R., 1987. A general equation for estimating Fe<sup>3+</sup> concentrations in ferromagnesian silicates and oxides from microprobe analyses, using stoichiometric criteria. *Mineralogical magazine* 51, 431–435.
- Dygert, N., Liang, Y., Sun, C., Hess, P., 2014. An experimental study of trace element partitioning between augite and Fe-rich basalts. *Geochimica et Cosmochimica Acta* 132, 170–186. doi:10.1016/j.gca.2014.01.042.
- Edgar, C.J., Wolff, J.A., Olin, P.H., Nichols, H.J., Pittari, A., Cas, R.A.F., Reiners, P.W., Spell, T.L., Martí, J., 2007. The late Quaternary Diego Hernandez Formation, Tenerife: Volcanology of a complex cycle of voluminous

- 1052      explosive phonolitic eruptions. *Journal of Volcanology and Geothermal Re-*  
1053      *search* 160, 59–85. doi:10.1016/j.jvolgeores.2006.06.001.
- 1054      Eugster, H.P., Wones, D.R., 1962. Stability relations of the ferruginous bi-
- 1055      otite, annite. *Journal of Petrology* 3, 82–125. doi:10.1093/petrology/3.1.82.
- 1056      Fedele, L., Lustrino, M., Melluso, L., Morra, V., Zanetti, A., Van-
- 1057      nucci, R., 2015. Trace-element partitioning between plagioclase, alkali
- 1058      feldspar, Ti-magnetite, biotite, apatite, and evolved potassic liquids from
- 1059      Campi Flegrei (Southern Italy). *American Mineralogist* 100, 233–249.
- 1060      doi:10.2138/am-2015-4995.
- 1061      Fedele, L., Zanetti, A., Morra, V., Lustrino, M., Melluso, L., Vannucci,
- 1062      R., 2009. Clinopyroxene/liquid trace element partitioning in natural
- 1063      trachyte–trachyphonolite systems: insights from Campi Flegrei (south-
- 1064      ern Italy). *Contributions to Mineralogy and Petrology* 158, 337–356.
- 1065      doi:10.1007/s00410-009-0386-5.
- 1066      Foley, S.F., Prelevic, D., Rehfeldt, T., Jacob, D.E., 2013. Minor and
- 1067      trace elements in olivines as probes into early igneous and mantle
- 1068      melting processes. *Earth and Planetary Science Letters* 363, 181–191.
- 1069      doi:10.1016/j.epsl.2012.11.025.
- 1070      Francis, D., Minarik, W., 2008. Aluminum-dependent trace element parti-
- 1071      tioning in clinopyroxene. *Contributions to Mineralogy and Petrology* 156,
- 1072      439–451. doi:10.1007/s00410-008-0295-z.
- 1073      Gaetani, G.A., 2004. The influence of melt structure on trace element par-

- 1074 titioning near the peridotite solidus. Contributions to Mineralogy and  
1075 Petrology 147, 511–527. doi:10.1007/s00410-004-0575-1.
- 1076 Gaetani, G.A., Grove, T.L., 1995. Partitioning of rare earth elements between  
1077 clinopyroxene and silicate melt: Crystal-chemical controls. Geochimica et  
1078 Cosmochimica Acta 59, 1951–1962. doi:10.1016/0016-7037(95)00119-0.
- 1079 Gaillard, F., Scaillet, B., Pichavant, M., 2002. Kinetics of iron oxidation-  
1080 reduction in hydrous silicic melts. American Mineralogist 87, 829–837.  
1081 doi:10.2138/am-2002-0704.
- 1082 Giehl, C., Marks, M., Nowak, M., 2013. Phase relations and liquid lines  
1083 of descent of an iron-rich peralkaline phonolitic melt: an experimen-  
1084 tal study. Contributions to Mineralogy and Petrology 165, 283–304.  
1085 doi:10.1007/s00410-012-0809-6.
- 1086 Giordano, D., Nichols, A., Dingwell, D., 2005. Glass transition temperatures  
1087 of natural hydrous melts: a relationship with shear viscosity and impli-  
1088 cations for the welding process. Journal of Volcanology and Geothermal  
1089 Research 142, 105–118. doi:10.1016/j.jvolgeores.2004.10.015.
- 1090 Girnis, A.V., Bulatov, V.K., Brey, G.P., Gerdes, A., Höfer, H.E., 2013. Trace  
1091 element partitioning between mantle minerals and silico-carbonate melts  
1092 at 6–12 GPa and applications to mantle metasomatism and kimberlite  
1093 genesis. Lithos 160–161, 183–200. doi:10.1016/j.lithos.2012.11.027.
- 1094 Goodenough, K.M., Schilling, J., Jonsson, E., Kalvig, P., Charles, N., Tuduri,  
1095 J., Deady, E.A., Sadeghi, M., Schiellerup, H., Müller, A., Bertrand, G.,  
1096 Arvanitidis, N., Eliopoulos, D.G., Shaw, R.A., Thrane, K., Keulen, N.,

- 1097      2016. Europe's rare earth element resource potential: An overview of  
1098      REE metallogenetic provinces and their geodynamic setting. *Ore Geology*  
1099      Reviews 72, 838–856. doi:10.1016/j.oregeorev.2015.09.019.
- 1100      Grove, T.L., Baker, M.B., Kinzler, R.J., 1984. Coupled CaAl-NaSi dif-  
1101      fusion in plagioclase feldspar: Experiments and applications to cooling  
1102      rate speedometry. *Geochimica et Cosmochimica Acta* 48, 2113–2121.  
1103      doi:10.1016/0016-7037(84)90391-0.
- 1104      Guillou, H., Carracedo, J.C., Paris, R., Pérèz Torrado, F.J., 2004. Implica-  
1105      tions for the early shield-stage evolution of Tenerife from K/Ar ages and  
1106      magnetic stratigraphy. *Earth and Planetary Science Letters* 222, 599–614.  
1107      doi:10.1016/j.epsl.2004.03.012.
- 1108      Gurenko, A.A., Hoernle, K.A., Hauff, F., Schmincke, H.U., Han, D., Miura,  
1109      Y.N., Kaneoka, I., 2006. Major, trace element and NdSrPbOHeAr isotope  
1110      signatures of shield stage lavas from the central and western Canary Is-  
1111      lands: Insights into mantle and crustal processes. *Chemical Geology* 233,  
1112      75–112. doi:10.1016/j.chemgeo.2006.02.016.
- 1113      Hanchar, J.M., Finch, R.J., Hoskin, P.W.O., Watson, E.B., Cher-  
1114      niak, D.J., Mariano, A.N., 2001. Rare earth elements in synthetic  
1115      zircon: Part 1. Synthesis, and rare earth element and phospho-  
1116      rus doping. *American Mineralogist* 86, 667–680. doi:10.1130/0091-  
1117      7613(1990)018;0757:CTOGAS;2.3.CO;2.
- 1118      Hazen, R.M., Finger, L.W., 1979. Bulk modulus-volume relationship for

- 1119 cation-anion polyhedra. *Journal of Geophysical Research: Solid Earth* 84,  
1120 6723–6728. doi:10.1029/JB084iB12p06723.
- 1121 Hill, E., Blundy, J.D., Wood, B.J., 2011. Clinopyroxene-melt trace ele-  
1122 ment partitioning and the development of a predictive model for HFSE  
1123 and Sc. *Contributions to Mineralogy and Petrology* 161, 423–438.  
1124 doi:10.1007/s00410-010-0540-0.
- 1125 Hill, E., Wood, B.J., Blundy, J.D., 2000. The effect of Ca-Tschermaaks com-  
1126 ponent on trace element partitioning between clinopyroxene and silicate  
1127 melt. *Lithos* 53, 203–215. doi:10.1016/S0024-4937(00)00025-6.
- 1128 Huang, F., Lundstrom, C.C., McDonough, W.F., 2006. Effect of melt  
1129 structure on trace-element partitioning between clinopyroxene and sili-  
1130 cic, alkaline, aluminous melts. *American Mineralogist* 91, 1385–1400.  
1131 doi:10.2138/am.2006.1909.
- 1132 Jugo, P.J., Wilke, M., Botcharnikov, R.E., 2010. Sulfur K-edge XANES anal-  
1133 ysis of natural and synthetic basaltic glasses: Implications for S speciation  
1134 and S content as function of oxygen fugacity. *Geochimica et Cosmochimica  
1135 Acta* 74, 5926–5938. doi:10.1016/j.gca.2010.07.022.
- 1136 Kennedy, A.K., Lofgren, G.E., Wasserburg, G.J., 1993. An experimental  
1137 study of trace element partitioning between olivine, orthopyroxene and  
1138 melt in chondrules: equilibrium values and kinetic effects. *Earth and Plan-  
1139 etary Science Letters* 115, 177–195. doi:10.1016/0012-821X(93)90221-T.
- 1140 Kogarko, L.N., 1990. Ore-forming potential of alkaline magmas. *Lithos* 26,  
1141 167–175. doi:10.1016/0024-4937(90)90046-4.

- 1142 Kovalenko, V.I., Hervig, R.L., Sheridan, M.F., 1988. Ion microprobe anal-  
1143 yses of trace elements in anorthoclase, hedenbergite, aenigmatite, quartz,  
1144 apatite and glass in pantellerite: evidence for high water contents in pan-  
1145 tellerite melt. American Mineralogist 73, 1038–1045.
- 1146 Kress, V.C., Carmichael, I.S.E., 1991. The compressibility of silicate liquids  
1147 containing Fe<sub>2</sub>O<sub>3</sub> and the effect of composition, temperature, oxygen fu-  
1148 gacity and pressure on their redox states. Contributions to Mineralogy and  
1149 Petrology 108, 82–92. doi:10.1007/BF00307328.
- 1150 Kumazawa, M., 1969. The elastic constants of single-crystal or-  
1151 thopyroxene. Journal of Geophysical Research 74, 5973–5980.  
1152 doi:10.1029/JB074i025p05973.
- 1153 Larsen, L.M., 1979. Distribution of REE and other trace elements between  
1154 phenocrysts and peralkaline undersaturated magmas, exemplified by rocks  
1155 from the Gardar igneous province, south Greenland. Lithos 12, 303–315.  
1156 doi:10.1016/0024-4937(79)90022-7.
- 1157 Law, K.M., Blundy, J.D., Wood, B.J., Ragnarsdottir, K.V., 2000. Trace ele-  
1158 ment partitioning between wollastonite and silicate-carbonate melt. Min-  
1159 eralogical Magazine 64, 651–661. doi:10.1180/002646100549670.
- 1160 Le Bas, M.J., Le Maitre, R.W., Streckeisen, A., Zanettin, B., 1986. A Chem-  
1161 ical Classification of Volcanic Rocks Based on the Total Alkali-Silica Dia-  
1162 gram. Journal of Petrology 27, 745–750. doi:10.1093/petrology/27.3.745.
- 1163 Liang, Y., Richter, F.M., Watson, E.B., 1994. Convection in multicom-

- 1164      ponent silicate melts driven by coupled diffusion. *Nature* 369, 390–392.  
1165      doi:10.1038/369390a0.
- 1166      Linnen, R.L., Keppler, H., 1997. Columbite solubility in granitic melts:  
1167      consequences for the enrichment and fractionation of Nb and Ta in the  
1168      Earth's crust. *Contributions to Mineralogy and Petrology* 128, 213–227.  
1169      doi:10.1007/s004100050304.
- 1170      Lofgren, G., 1989. Dynamic crystallization of chondrule melts of porphyritic  
1171      olivine composition: Textures experimental and natural. *Geochimica et  
1172      Cosmochimica Acta* 53, 461–470. doi:10.1016/0016-7037(89)90397-9.
- 1173      Lofgren, G.E., Huss, G.R., Wasserburg, G.J., 2006. An experimental study  
1174      of trace-element partitioning between Ti-Al-clinopyroxene and melt: Equi-  
1175      librium and kinetic effects including sector zoning. *American Mineralogist*  
1176      91, 1596–1606. doi:10.2138/am.2006.2108.
- 1177      Lu, F., Anderson, A.T., Davis, A.M., 1995. Diffusional gradients at the crys-  
1178      tal / melt interface and their effect on the compositions of melt inclusions.  
1179      *The Journal of Geology* 103, 591–597.
- 1180      Lundstrom, C.C., Shaw, H.F., Ryerson, F.J., Phinney, D.L., Gill, J.B.,  
1181      Williams, Q., 1994. Compositional controls on the partitioning of U, Th,  
1182      Ba, Pb, Sr and Zr between clinopyroxene and haplobasaltic melts: impli-  
1183      cations for uranium series disequilibria in basalts. *Earth and Planetary  
1184      Science Letters* 128, 407–423. doi:10.1016/0012-821X(94)90159-7.
- 1185      Mahood, G.A., Stimac, J.A., 1990. Trace-element partitioning in panta-

- 1186      lerites and trachytes. *Geochimica et Cosmochimica Acta* 54, 2257–2276.  
1187      doi:10.1016/0016-7037(90)90050-U.
- 1188      Marks, M., Halama, R., Wenzel, T., Markl, G., 2004. Trace element vari-  
1189      ations in clinopyroxene and amphibole from alkaline to peralkaline syen-  
1190      ites and granites: implications for mineral-melt trace-element partitioning.  
1191      *Chemical Geology* 211, 185–215. doi:10.1016/j.chemgeo.2004.06.032.
- 1192      Marks, M., Markl, G., 2001. Fractionation and assimilation processes in the  
1193      alkaline augite syenite unit of the Ilímaussaq intrusion, south Greenland,  
1194      as deduced from phase equilibria. *Journal of Petrology* 42, 1947–1969.  
1195      doi:10.1093/petrology/42.10.1947.
- 1196      Marks, M., Markl, G., 2003. Ilímaussaq en miniature': closed-system frac-  
1197      tionation in an agpaitic dyke rock from the Gardar Province, South Green-  
1198      land (contribution to the mineralogy of Ilímaussaq no. 117). *Mineralogical*  
1199      *Magazine* 67, 893–919. doi:10.1180/0026461036750150.
- 1200      Marks, M.A., Markl, G., 2017. A global review on agpaitic rocks. *Earth-*  
1201      *Science Reviews* 173, 229–258. doi:10.1016/j.earscirev.2017.06.002.
- 1202      Marks, M.A.W., Hettmann, K., Schilling, J., Frost, B.R., Markl, G., 2011.  
1203      The mineralogical diversity of alkaline igneous rocks: Critical factors for  
1204      the transition from miaskitic to agpaitic phase assemblages. *Journal of*  
1205      *Petrology* 52, 439–455. doi:10.1093/petrology/eqq086.
- 1206      Möller, V., Williams-Jones, A.E., 2016. Petrogenesis of the Nеча-  
1207      lacho Layered Suite, Canada: magmatic Evolution of a REE-Nb-

- 1208 rich Nepheline Syenite Intrusion. *Journal of Petrology* 57, 229–276.  
1209 doi:10.1093/petrology/egw003.
- 1210 Mollo, S., Blundy, J.D., Giacomoni, P., Nazzari, M., Scarlato, P., Coltorti,  
1211 M., Langone, A., Andronico, D., 2017. Clinopyroxene-melt element par-  
1212 titioning during interaction between trachybasaltic magma and siliceous  
1213 crust: Clues from quartzite enclaves at Mt. Etna volcano. *Lithos* 284–285,  
1214 447–461. doi:10.1016/j.lithos.2017.05.003.
- 1215 Mollo, S., Blundy, J.D., Iezzi, G., Scarlato, P., Langone, A., 2013. The  
1216 partitioning of trace elements between clinopyroxene and trachybasaltic  
1217 melt during rapid cooling and crystal growth. *Contributions to Mineralogy  
1218 and Petrology* 166, 1633–1654. doi:10.1007/s00410-013-0946-6.
- 1219 Mollo, S., Forni, F., Bachmann, O., Blundy, J.D., De Astis, G., Scarlato,  
1220 P., 2016. Trace element partitioning between clinopyroxene and trachy-  
1221 phonolitic melts: A case study from the Campanian Ignimbrite (Campi  
1222 Flegrei, Italy). *Lithos* 252253, 160–172. doi:10.1016/j.lithos.2016.02.024.
- 1223 Moore, G., Vennemann, T., Carmichael, I.S.E., 1998. An empirical model  
1224 for the solubility of H<sub>2</sub>O in magmas to 3 kilobars. *American Mineralogist*  
1225 83, 36–42. doi:10.1016/0012-821X(73)90129-5.
- 1226 Morimoto, N., 1989. Nomenclature of pyroxenes. *Mineralogical Journal* 14,  
1227 198–221. doi:10.2465/minerj.14.198.
- 1228 Mungall, J., Brenan, J., 2014. Partitioning of platinum-group elements and  
1229 Au between sulfide liquid and basalt and the origins of mantle-crust frac-

- 1230 tination of the chalcophile elements. *Geochimica et Cosmochimica Acta*  
1231 125, 265–289. doi:10.1016/j.gca.2013.10.002.
- 1232 Mysen, B.O., Virgo, D., Seifert, F.A., 1982. The structure of silicate melts:  
1233 Implications for chemical and physical properties of natural magma. *Re-*  
1234 *views of Geophysics* 20, 353–383. doi:10.1029/RG020i003p00353.
- 1235 Mysen, B.O., Virgo, D., Seifert, F.A., 1985. Relationships between properties  
1236 and structure of aluminosilicate melts. *American Mineralogist* 70, 88–105.  
1237 doi:10.1007/BF00413348.
- 1238 Niu, Y., 2004. Bulk-rock major and trace element compositions of abyssal  
1239 peridotites: Implications for mantle melting, melt extraction and post-  
1240 melting processes beneath Mid-Ocean ridges. *Journal of Petrology* 45,  
1241 2423–2458. doi:10.1093/petrology/egh068.
- 1242 Olin, P.H., Wolff, J.A., 2010. Rare earth and high field strength element par-  
1243 titioning between iron-rich clinopyroxenes and felsic liquids. *Contributions*  
1244 *to Mineralogy and Petrology* 160, 761–775. doi:10.1007/s00410-010-0506-2.
- 1245 Onuma, N., Higuchi, H., Wakita, H., Nagasawa, H., 1968. Trace element  
1246 partition between two pyroxenes and the host lava. *Earth and Planetary*  
1247 *Science Letters* 5, 47–51. doi:10.1016/S0012-821X(68)80010-X.
- 1248 Paton, C., Hellstrom, J., Paul, B., Woodhead, J., Herdt, J., 2011. Io-  
1249 lite: Freeware for the visualisation and processing of mass spectromet-  
1250 ric data. *Journal of Analytical Atomic Spectrometry* 26, 2508–2518.  
1251 doi:10.1039/C1JA10172B.

- 1252 Peters, S.T., Troll, V.R., Weis, F.A., Dallai, L., Chadwick, J.P., Schulz, B.,  
1253 2017. Amphibole megacrysts as a probe into the deep plumbing system  
1254 of Merapi volcano, Central Java, Indonesia. Contributions to Mineralogy  
1255 and Petrology 172, 1–20. doi:10.1007/s00410-017-1338-0.
- 1256 Prowatke, S., Klemme, S., 2005. Effect of melt composition on the parti-  
1257 tioning of trace elements between titanite and silicate melt. Geochimica  
1258 et Cosmochimica Acta 69, 695–709. doi:10.1016/j.gca.2004.06.037.
- 1259 Putirka, K.D., 2008. Thermometers and Barometers for Volcanic  
1260 Systems. Reviews in Mineralogy and Geochemistry 69, 61–120.  
1261 doi:10.2138/rmg.2008.69.3.
- 1262 Rapp, R.P., Watson, E.B., 1986. Monazite solubility and dissolution ki-  
1263 netics: implications for the thorium and light rare earth chemistry of  
1264 felsic magmas. Contributions to Mineralogy and Petrology 94, 304–316.  
1265 doi:10.1007/BF00371439.
- 1266 Rasband, W., 2016. ImageJ, U.S. National Institutes of Health, Bethesda,  
1267 Maryland, USA.
- 1268 Redhammer, G.J., Amthauer, G., Roth, G., Tippelt, G., Lotter-  
1269 moser, W., 2006. Single-crystal X-ray diffraction and temperature  
1270 dependent  $^{57}\text{Fe}$  Mössbauer spectroscopy on the hedenbergite-aegirine  
1271  $(\text{Ca},\text{Na})(\text{Fe}^{2+},\text{Fe}^{3+})\text{Si}_2\text{O}_6$  solid solution. American Mineralogist 91,  
1272 1271–1292. doi:10.2138/am.2006.2173.
- 1273 Reguir, E.P., Chakhmouradian, A.R., Pisiak, L., Halden, N.M., Yang, P.,  
1274 Xu, C., Kynický, J., Couëslan, C.G., 2012. Trace-element composition

- 1275 and zoning in clinopyroxene- and amphibole-group minerals: Implications  
1276 for element partitioning and evolution of carbonatites. *Lithos* 128, 27–45.  
1277 doi:10.1016/j.lithos.2011.10.003.
- 1278 Rubatto, D., Hermann, J., 2007. Experimental zircon/melt and  
1279 zircon/garnet trace element partitioning and implications for the  
1280 geochronology of crustal rocks. *Chemical Geology* 241, 38–61.  
1281 doi:10.1016/j.chemgeo.2007.01.027.
- 1282 Schmidt, B.C., Behrens, H., 2008. Water solubility in phonolite melts: Influ-  
1283 ence of melt composition and temperature. *Chemical Geology* 256, 259–  
1284 268. doi:10.1016/j.chemgeo.2008.06.043.
- 1285 Schmidt, K.H., Bottazzi, P., Vannucci, R., Mengel, K., 1999. Trace element  
1286 partitioning between phlogopite, clinopyroxene and leucite lamproite melt.  
1287 *Earth and Planetary Science Letters* 168, 287–299. doi:10.1016/S0012-  
1288 821X(99)00056-4.
- 1289 Schmidt, M.W., Connolly, J.A.D., Günther, D., Bogaerts, M., 2006. Element  
1290 partitioning: The role of melt structure and composition. *Science* 312,  
1291 1646–1650. doi:10.1126/science.1126690.
- 1292 Severs, M.J., Beard, J.S., Fedele, L., Hanchar, J.M., Mutchler, S.R., Bodnar,  
1293 R.J., 2009. Partitioning behavior of trace elements between dacitic melt  
1294 and plagioclase, orthopyroxene, and clinopyroxene based on laser ablation  
1295 ICPMS analysis of silicate melt inclusions. *Geochimica et Cosmochimica  
1296 Acta* 73, 2123–2141. doi:10.1016/j.gca.2009.01.009.

- 1297 Shannon, R., 1976. Revised effective ionic radii and systematic studies of  
1298 interatomic distances in halides and chalcogenides. *Acta Crystallographica*  
1299 Section A 32, 751–767.
- 1300 Shea, T., Hammer, J.E., 2013. Kinetics of cooling- and decompression-  
1301 induced crystallization in hydrous mafic-intermediate magmas.  
1302 *Journal of Volcanology and Geothermal Research* 260, 127–145.  
1303 doi:10.1016/j.jvolgeores.2013.04.018.
- 1304 Shearer, C.K., Larsen, L.M., 1994. Sector-zoned aegirine from the Ilimaussaq  
1305 alkaline intrusion, South Greenland; implications for trace-element behav-  
1306 ior in pyroxene. *American Mineralogist* 79, 340–352.
- 1307 Sjöqvist, A., Cornell, D., Andersen, T., Erambert, M., Ek, M., Leijd, M.,  
1308 2013. Three compositional varieties of rare-earth element ore: Eudialyte-  
1309 group minerals from the Norra Kärr alkaline complex, Southern Sweden.  
1310 *Minerals* 3, 94–120. doi:10.3390/min3010094.
- 1311 Sørensen, H., 1992. Agpaitic nepheline syenites: a potential source of  
1312 rare elements. *Applied Geochemistry* 7, 417–427. doi:10.1016/0883-  
1313 2927(92)90003-L.
- 1314 Spera, F.J., Bohrson, W.A., 2001. Energy-constrained open-system mag-  
1315 matic processes I: General model and energy-constrained assimilation and  
1316 fractional crystallization (EC-AFC) formulation. *Journal of Petrology* 42,  
1317 999–1018. doi:10.1093/petrology/42.5.999.
- 1318 Stevens, J., 1996. Applied multivariate analysis for the social sciences.  
1319 Lawrence Erlbaum, Mahwah, NJ.

- 1320 Sun, C., Liang, Y., 2012. Distribution of REE between clinopyroxene and  
1321 basaltic melt along a mantle adiabat: Effects of major element composi-  
1322 tion, water, and temperature. Contributions to Mineralogy and Petrology  
1323 163, 807–823. doi:10.1007/s00410-011-0700-x.
- 1324 Thirlwall, M.F., Singer, B.S., Marriner, G.F., 2000.  $^{39}\text{Ar}$ – $^{40}\text{Ar}$  ages and  
1325 geochemistry of the basaltic shield stage of Tenerife, Canary Islands,  
1326 Spain. Journal of Volcanology and Geothermal Research 103, 247–297.  
1327 doi:10.1016/S0377-0273(00)00227-4.
- 1328 Troll, V., Schmincke, H., 2002. Magma mixing and crustal recycling recorded  
1329 in ternary feldspar from compositionally zoned peralkaline ignimbrite  
1330 'A', Gran Canaria, Canary Islands. Journal of Petrology 43, 243–270.  
1331 doi:10.1093/petrology/43.2.243.
- 1332 Van Orman, J.A., Grove, T.L., Shimizu, N., 2001. Rare earth element diffu-  
1333 sion in diopside: influence of temperature, pressure, and ionic radius, and  
1334 an elastic model for diffusion in silicates. Contributions to Mineralogy and  
1335 Petrology 141, 687–703. doi:10.1007/s004100100269.
- 1336 Walker, D., Kirkpatrick, R.J., Longhi, J., Hays, J.F., 1976. Crystallization  
1337 history of lunar picritic basalt sample 12002: Phase-equilibria and cooling-  
1338 rate studies. Bulletin of the Geological Society of America 87, 646–656.  
1339 doi:10.1130/0016-7606.
- 1340 Watson, E.B., 1979. Zircon saturation in felsic liquids: Experimental results  
1341 and applications to trace element geochemistry. Contributions to Miner-  
1342 alogy and Petrology 70, 407–419. doi:10.1007/BF00371047.

- 1343 Weidner, D.J., Vaughan, M.T., 1982. Elasticity of pyroxenes: Effects of  
1344 composition versus crystal structure. *Journal of Geophysical Research* 87,  
1345 9349–9353.
- 1346 Wiesmaier, S., Troll, V.R., Carracedo, J.C., Ellam, R.M., Bindeman, I.,  
1347 Wolff, J.A., 2012. Bimodality of lavas in the Teide–Pico Viejo Succession  
1348 in Tenerife—the role of crustal melting in the origin of recent phonolites.  
1349 *Journal of Petrology* 53, 2465–2495. doi:10.1093/petrology/egs056.
- 1350 Wood, B.J., Blundy, J.D., 1997. A predictive model for rare earth  
1351 element partitioning between clinopyroxene and anhydrous silicate  
1352 melt. *Contributions to Mineralogy and Petrology* 129, 166–181.  
1353 doi:10.1007/s004100050330.
- 1354 Wood, B.J., Blundy, J.D., 2001. The effect of cation charge on crystal–melt  
1355 partitioning of trace elements. *Earth and Planetary Science Letters* 188,  
1356 59–71. doi:10.1016/S0012-821X(01)00294-1.
- 1357 Wood, B.J., Blundy, J.D., 2003. Trace element partitioning under crustal  
1358 and uppermost mantle conditions: The influences of ionic radius, cation  
1359 charge, pressure, and temperature, in: Carlson, R.W. (Ed.), *The Mantle*  
1360 and Core: Treatise on Geochemistry. Elsevier. volume 2. chapter 2.09, pp.  
1361 395–424. doi:10.1016/B0-08-043751-6/02009-0.
- 1362 Wood, B.J., Blundy, J.D., 2014. Trace element partitioning: The influences  
1363 of ionic radius, cation charge, pressure, and temperature, in: Carlson,  
1364 R.W. (Ed.), *The Mantle and Core: Treatise on Geochemistry: Second Edi-*

- 1365 tion. Elsevier. chapter 3.11, pp. 421–445. doi:10.1016/B978-0-08-095975-  
1366 7.00206-0.
- 1367 Wood, B.J., Trigila, R., 2001. Experimental determination of aluminous  
1368 clinopyroxene–melt partition coefficients for potassic liquids, with applica-  
1369 tion to the evolution of the Roman province potassic magmas. Chemical  
1370 Geology 172, 213–223. doi:10.1016/S0009-2541(00)00259-X.
- 1371 Workman, R.K., Hart, S.R., 2005. Major and trace element composition of  
1372 the depleted MORB mantle (DMM). Earth and Planetary Science Letters  
1373 231, 53–72. doi:10.1016/j.epsl.2004.12.005.
- 1374 Wörner, G., Beusen, J.M., Duchateau, N., Gijbels, R., Schmincke, H.U.,  
1375 1983. Trace element abundances and mineral/melt distribution coefficients  
1376 in phonolites from the Laacher See volcano (Germany). Contributions to  
1377 Mineralogy and Petrology 84, 152–173. doi:10.1007/BF00371282.
- 1378 Xu, C., Kynicky, J., Chakhmouradian, A.R., Campbell, I.H., Allen, C.M.,  
1379 2010. Trace-element modeling of the magmatic evolution of rare-earth-rich  
1380 carbonatite from the Miaoya deposit, Central China. Lithos 118, 145–155.  
1381 doi:10.1016/j.lithos.2010.04.003.
- 1382 Yang, L., van Hinsberg, V.J., Samson, I.M., 2018. A new method to decon-  
1383 volute binary mixture in LA-ICP-MS analyses to quantify the composition  
1384 of phases smaller than the laser spot size. JAAS .
- 1385 Yao, L., Sun, C., Liang, Y., 2012. A parameterized model for REE distri-  
1386 bution between low-Ca pyroxene and basaltic melts with applications to

<sub>1387</sub> REE partitioning in low-Ca pyroxene along a mantle adiabat and dur-  
<sub>1388</sub> ing pyroxenite-derived melt and peridotite interaction. Contributions to  
<sub>1389</sub> Mineralogy and Petrology 164, 261–280. doi:10.1007/s00410-012-0737-5.

<sub>1390</sub> Zhang, Y., Ni, H., Chen, Y., 2010. Diffusion data in silicate melts. Reviews  
<sub>1391</sub> in Mineralogy and Geochemistry 72, 311–408. doi:10.2138/rmg.2010.72.8.

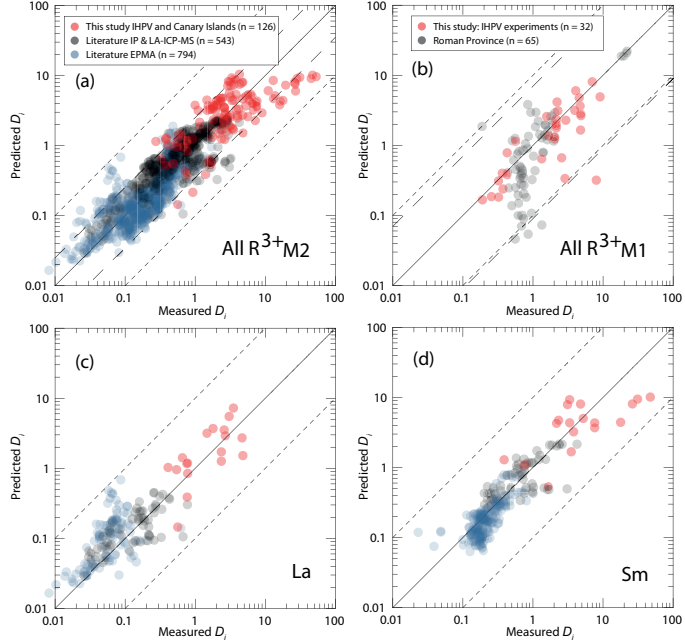


Figure 13: Measured clinopyroxene–silicate melt partition coefficients for 3+ cations vs. those predicted by our empirical model. (a) shows a comparison between measured partition coefficients and model-derived values for the M2 site of clinopyroxene. Hard dashed lines represent 95% confidence intervals of the model, and correspond to maximum uncertainties of factor  $\pm 2.5$ . Fine dashed lines represent 1 order of magnitude uncertainty (extreme outliers for M2 model). Partition coefficients in this diagram are the REE La to Er for our IHPV experiments, Canary Islands rocks, and literature data from the Roman Province (Wood and Trigila, 2001; Fedele et al., 2009; Mollo et al., 2013, 2016), and all the REE plus Y for the rest of the data compilation (Bédard, 2014), which is split by analytical methodology. (b) shows performance of the predictive model for the M1 site that is calibrated for alkaline magmatic systems, and includes data from our IHPV experiments and the Roman Province (Fedele et al., 2009; Mollo et al., 2013, 2016). Maximum uncertainties at the 95% confidence interval are a factor of  $\pm 7$ , higher than for the M2 site because of the smaller calibrating data set. (c) performance of the M2 site model for La, and (d) for Sm.

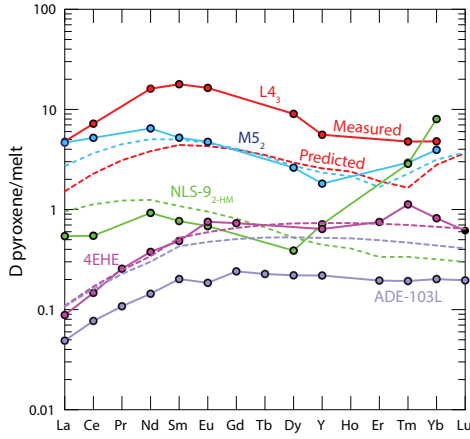


Figure 14: Measured and predicted element-partition coefficients for  $\text{REE}^{3+}$ . The model does not introduce notable radius-dependent biases, except for in our high-aegirine clinopyroxene (NLS-9<sub>2</sub>-HM in green) for which  $D_{\text{HREE}}$  are strongly underpredicted, owing to inaccurate return of  $D_0^{\text{M1}}$ . Shown for comparison are two diopside-melt pairs: 4EHE from Hill et al. (2000), grown from a synthetic (NCMAS) basaltic andesite composition and ADE-103L from Lofgren et al. (2006) grown from a picritic composition based on the Angra dos Reis meteorite.

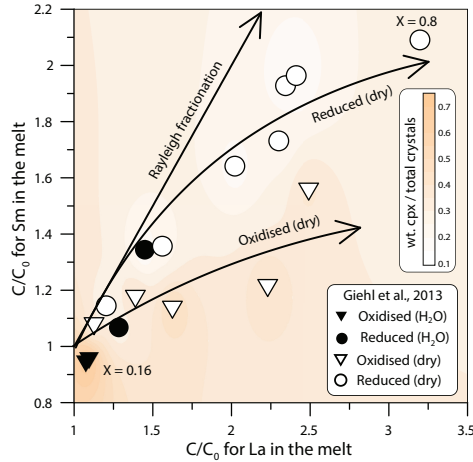


Figure 15: Model enrichment paths for La and Sm in residual melts during fractional crystallisation of a MiKa dyke composition (Gardar Province, Greenland, see Marks and Markl 2003). Phase relations and clinopyroxene compositions are from Giehl et al. (2013) and pertain to both oxidising and reducing conditions ( $\log f\text{O}_2 = \Delta\text{QFM} - 3$  and +1), nominally dry to water bearing (to 3 wt.%  $\text{H}_2\text{O}$  at 1 kbar). Colour shading indicates the weight fraction of clinopyroxene within the crystallising assemblage. Bold arrows indicate residual enrichment pathways for the REE in the melt for Rayleigh fractionation (no incorporation into crystals), reduced, dry conditions, and oxidised dry conditions (the latter two are hand drawn fits to the data). For simplicity, this model does not consider REE incorporation into magnetite, alkali-feldspar, olivine, nepheline or aenigmatite, all phases generated in the experiments of Giehl et al. (2013) (see Larsen, 1979; Kovalenko et al., 1988; Mahood and Stimac, 1990).

<sup>1392</sup> **6. Tables**

Table 1: Major-element composition (in wt%) of starting materials for the internally heated pressure vessel experiments. The totals are calculated with all iron as FeO.

*Dry starting glass compositions calculated from masses of reagents added [wt%]*

Composition	SiO <sub>2</sub>	TiO <sub>2</sub>	Al <sub>2</sub> O <sub>3</sub>	FeOT	MgO	CaO	Na <sub>2</sub> O	K <sub>2</sub> O	Total	(Na+K)/Al
L4	57.48	1.50	19.00	5.89	1.61	3.21	7.33	3.98	100.00	0.861
L5	61.24	0.68	19.51	3.77	0.43	0.91	8.63	4.84	100.00	0.996
M3	52.67	2.27	18.13	7.86	2.75	5.40	7.19	3.73	100.00	0.875
M4	56.35	1.47	18.63	5.77	1.58	3.15	8.48	4.57	100.00	1.014
M5	60.04	0.66	19.13	3.69	0.42	0.89	9.76	5.41	100.00	1.145
H4	54.80	1.43	18.12	5.62	1.54	3.06	10.07	5.38	100.00	1.236
H5	58.38	0.65	18.60	3.59	0.41	0.86	11.31	6.20	100.00	1.362

*Water saturated glass compositions from superliquidus experiments (EPMA) [wt%]*

L5	57.46	0.643	16.59	2.363	0.404	0.985	7.840	4.462	90.75	1.069
s.d. (n = 8)	0.299	0.087	0.210	0.059	0.035	0.050	0.175	0.132	0.351	0.017
rsd	0.52%	13.58%	1.26%	2.51%	8.70%	5.09%	2.23%	2.97%	0.39%	1.57%
H5	55.58	0.612	16.21	2.568	0.422	0.906	10.77	5.732	92.80	1.476
s.d. (n = 13)	0.327	0.057	0.221	0.113	0.044	0.049	0.205	0.154	0.417	0.028
rsd	0.59%	9.33%	1.36%	4.41%	10.44%	5.40%	1.90%	2.69%	0.45%	1.87%

Table 2: Summary of run conditions and run products for the internally-heated pressure vessel experiments.

Experiment	Setup	Pressure [bar]	Cooling ramp				(after ramp) [h,m]	Run products
			Rate °C /min	Cycle +10°C	TE-1/TE-3 [°C ]	TE-2 (spl) [°C ]		
L4 <sub>3</sub>	IHPV RQ (f)	2038	1	Y	825	828	44h50m	Cpx + Ox + Ttn + Melt
L5 <sub>3</sub>	IHPV RQ (f)	2038	1	Y	825	828	44h50m	Cpx + Ox + Melt
M3 <sub>2</sub>	IHPV RQ	2020	1	Y	796/795	799	47h	Cpx + Ox + Bt + Melt
M4 <sub>4</sub>	IHPV RQ	2020	1	Y	796/795	799	47h	Cpx + Ox + Bt + Melt
M5	IHPV	2000	-	-	800	799	47h55m	Cpx + Bt + Fsp + Melt
M5 <sub>2</sub>	IHPV RQ	2000	-	-	700	689	45h45m	Cpx + Bt + Fsp + Melt
H4 <sub>2</sub>	IHPV	2000	-	-	800	799	47h55m	Cpx + Ttn + Melt
H5 <sub>2</sub>	IHPV RQ	2000	-	-	700	689	45h45m	Cpx + Bt + Fsp + Melt
H5 <sub>3</sub>	IHPV RQ	2020	-	-	651/649	648	46h15m	Cpx + Bt + Fsp + Melt
NLS-9	IHPV RQ	2020	1	Y	651/649	648	46h15m	Cpx + Ox + Melt
NLS-9 <sub>2</sub> HM	IHPV RQ**	2000	1	Y	650	655	42h	Cpx + Ox + Fsp + Melt

(f) indicates failure of the rapid quench apparatus; \*\* indicates use of a haematite double capsule, for run conditions at the haematite-magnetite  $f\text{O}_2$  buffer (Eugster and Wones, 1962). Cpx = clinopyroxene; Ox = spinel oxide; Ttn = titanite; Bt = biotite; Fsp = sanidine feldspar.

Table 3: Representative major-element compositions of clinopyroxene and melt for the performed internally heated pressure vessel experiments and Canary Islands phenocryst–glass pairs.

<i>Pyroxene</i>	L4 <sub>3</sub>	M3 <sub>2</sub>	M5 <sub>2</sub>	H5 <sub>3</sub>	NLS-9	NLS-9 <sub>2</sub> HM	16-07 LMB	17-12 M. Samara	17-14 UMB-II	21-30 PV 2 ka
SiO <sub>2</sub>	44.70	40.73	47.31	46.95	50.73	51.90	52.43	51.77	51.81	52.50
TiO <sub>2</sub>	3.07	4.57	3.17	4.47	0.10	0.10	0.80	0.78	0.74	0.75
Al <sub>2</sub> O <sub>3</sub>	5.23	9.26	3.08	3.10	2.46	2.96	1.33	1.24	1.27	1.22
FeO	13.31	11.72	18.84	16.95	28.14	28.61	9.71	9.62	10.51	10.02
MnO	0.01	0.01	0.01	0.00	0.25	0.17	0.78	0.84	0.91	0.81
MgO	9.09	9.28	5.55	6.05	0.05	0.07	12.30	12.64	12.07	11.88
CaO	19.49	22.17	16.11	15.29	5.88	3.14	21.90	21.76	21.52	22.02
Na <sub>2</sub> O	2.27	1.01	4.34	4.97	9.86	11.45	1.18	1.17	1.38	1.19
K <sub>2</sub> O	0.09	0.03	0.08	0.07	0.04	0.04	0.02	0.03	0.00	0.02
Total	97.25	98.78	98.49	97.85	97.49	98.45	100.44	99.85	100.22	100.42
<i>Glass</i>										
SiO <sub>2</sub>	58.79	57.29	57.45	54.91	58.17	58.14	60.38	55.10	59.08	60.04
TiO <sub>2</sub>	0.35	0.27	0.23	0.62	0.00	0.00	0.64	1.73	0.66	0.66
Al <sub>2</sub> O <sub>3</sub>	17.35	19.14	16.69	16.06	18.55	19.41	19.96	18.30	19.68	19.79
Fe <sub>2</sub> O <sub>3</sub> (T)	2.35	1.35	1.01	3.16	1.67	1.91	3.65	7.22	4.02	3.96
FeO(T)	2.12	1.22	0.91	2.84	1.50	1.72	3.28	6.49	3.62	3.56
MnO	0.02	0.00	-	0.01	0.06	0.04	0.14	0.23	0.22	0.20
MgO	0.20	0.13	0.15	0.35	0.00	0.00	0.39	1.84	0.32	0.35
CaO	0.55	0.95	0.24	0.84	0.23	0.23	0.76	4.10	0.77	0.74
Na <sub>2</sub> O	7.17	7.32	9.08	8.88	11.12	9.80	9.00	7.26	9.76	9.05
K <sub>2</sub> O	4.68	4.10	4.68	5.30	1.51	2.51	5.41	4.09	5.45	5.57
Total	91.23	90.41	89.43	89.81	91.15	91.85	99.95	99.13	99.56	99.95
(Na+K)/Al	0.97	0.86	1.15	1.27	1.07	0.97	1.01	1.12	1.09	1.09

Table 4: Pyroxene-melt trace-element-partition coefficients for representative experiments and a natural phenocryst-glass pair.

-	L4 <sub>3</sub>		M3 <sub>2</sub>		M5 <sub>2</sub>		H5 <sub>3</sub>		NLS-9		NLS-9 <sub>2</sub> HM		16-07-px4 LMB	
	D	$\sigma$	D	$\sigma$	D	$\sigma$	D	$\sigma$	D	$\sigma$	D	$\sigma$	D	$\sigma$
Li	0.250	0.016	0.126	0.009	0.419	0.034	0.427	0.024	0.274	0.029	0.251	0.025	0.157	0.021
Ga	0.364	0.022	0.567	0.020	0.190	0.022	-	-	-	-	-	-	0.216	0.020
Rb	0.005	0.002	0.018	0.003	0.010	0.006	0.013	0.002	0.026	0.015	-	-	0.000	0.000
Sr	0.828	0.045	0.282	0.024	1.433	0.111	0.997	0.091	0.321	0.045	0.269	0.111	0.732	0.293
Y	5.577	0.302	13.784	1.949	1.814	0.236	1.102	0.060	0.482	0.048	0.713	0.070	2.183	0.232
Zr	1.699	0.082	2.537	0.222	1.361	0.089	1.164	0.083	2.102	0.196	3.895	0.482	0.434	0.047
Nb	0.126	0.085	0.889	0.258	0.554	0.280	1.688	0.196	2.382	0.294	9.642	4.015	0.0062	0.0004
Cs	0.019	0.003	0.019	0.003	0.014	0.006	0.010	0.002	-	-	0.023	0.017	0.001	0.001
Ba	0.0364	0.0087	0.0373	0.0152	0.0388	0.0261	0.0288	0.0091	-	-	-	-	0.00004	0.00004
La	4.787	0.646	2.591	0.240	4.658	0.962	3.049	0.132	0.410	0.037	0.542	0.043	0.769	0.071
Ce	7.199	0.756	6.229	0.646	5.199	1.073	3.190	0.129	0.377	0.028	0.547	0.061	1.591	0.120
Nd	16.105	1.537	28.430	4.210	6.454	1.630	3.759	0.147	0.579	0.054	0.925	0.114	2.632	0.155
Sm	17.843	1.414	47.245	7.699	5.215	1.293	3.113	0.137	0.388	0.070	0.767	0.182	3.522	0.421
Eu	16.403	1.341	53.195	8.181	4.743	1.132	2.900	0.133	0.275	0.082	0.682	0.192	3.372	0.196
Dy	9.027	0.537	27.082	3.925	2.619	0.460	1.521	0.073	0.329	0.057	0.388	0.088	2.798	0.220
Tm	4.773	0.261	9.067	0.903	2.937	0.279	1.567	0.097	1.330	0.145	2.860	0.890	1.846	0.182
Yb	4.797	0.249	7.015	0.600	3.937	0.296	2.281	0.152	2.564	0.346	8.004	3.116	1.978	0.186
Hf	2.385	0.162	3.556	0.472	1.802	0.118	1.141	0.123	2.443	0.275	3.702	0.479	0.769	0.065
Ta	0.496	0.152	2.3694	0.6244	0.6502	0.2545	1.5654	0.2337	2.1082	0.1764	3.6854	0.6561	0.0153	0.0013
Pb	0.079	0.017	0.0587	0.0152	0.1142	0.0349	0.0199	0.0130	0.0884	0.0280	0.0564	0.0536	0.0203	0.0040
Th	0.201	0.034	0.3565	0.0419	0.3172	0.0321	0.2892	0.0239	0.0798	0.0240	0.0709	0.0276	0.0040	0.0003
U	-	-	0.0512	0.0331	0.1261	0.0272	0.0196	0.0103	0.0460	0.0245	0.0834	0.0342	0.0022	0.0003

Table 5: Coefficients for prediction of lattice-strain parameters for clinopyroxene M1 and M2 sites from clinopyroxene composition, temperature and pressure. Fitted vs. predicted lattice-strain parameters and partition coefficients are in Figures 12–13 and full multiple linear regression reports are available as supplementary data file S4.

Model for $\text{Ln}D_0$ M2 site (n = 82)			Model for $\text{Ln}D_0$ , M1 site (n = 16)		
Parameter	Coefficient	$\sigma$	Parameter	Coefficient	$\sigma$
Intercept	4.52	0.91	Intercept	5	1
M1Ti	6.8	3	TAl	4	0.5
M1Al - M1Fe <sup>3+</sup>	1.6	0.6	M1Fe <sup>2+</sup>	2.6	0.9
M2Fe <sup>2+</sup>	-3.8	1.3	M2Na	-8	1
T [K]	-0.0035	0.0007	M2Ca	-3	2
TAl + TFe <sup>3+</sup>	2.6	0.8			
$R^2$		0.647			0.959

Model for $E_s$ , M2 site (n = 79)			Model for $E_s$ , M1 site (n = 18)		
Parameter	Coefficient	$\sigma$	Parameter	Coefficient	$\sigma$
Intercept	247	44	Intercept	-2322	298
M1Al	-424	144	T [K]	3.2	0.4
M1Mg	-285	102	P [GPa]	-408	145
M1Ti	-1145	378	M1Mg	-800	212
M2Mg	-306	115			
P [GPa]	37	12			
TAl + TFe <sup>3+</sup>	313	102			
XMg	336	102			
$R^2$		0.348			0.936

Model for $r_0$ , M2 site (n = 82)			Model for $r_0$ , M1 site (n = 16)		
Parameter	Coefficient	$\sigma$	Parameter	Coefficient	$\sigma$
Intercept	1.01	0.02	Intercept	0.79	0.03
M1Ti	0.16	0.05	P [GPa]	-0.017	0.005
M1Al-M1Fe <sup>3+</sup>	-0.03	0.01	M2Mg	-0.48	0.06
M2Ca	0.09	0.02	M1Fe <sup>3+</sup>	0.14	0.03
M2Na	0.14	0.02	M2Ca	-0.05	0.02
T [K]	-4.46E-05	1.22E-05			
$R^2$		0.846			0.987

1393 7. Supplementary figures

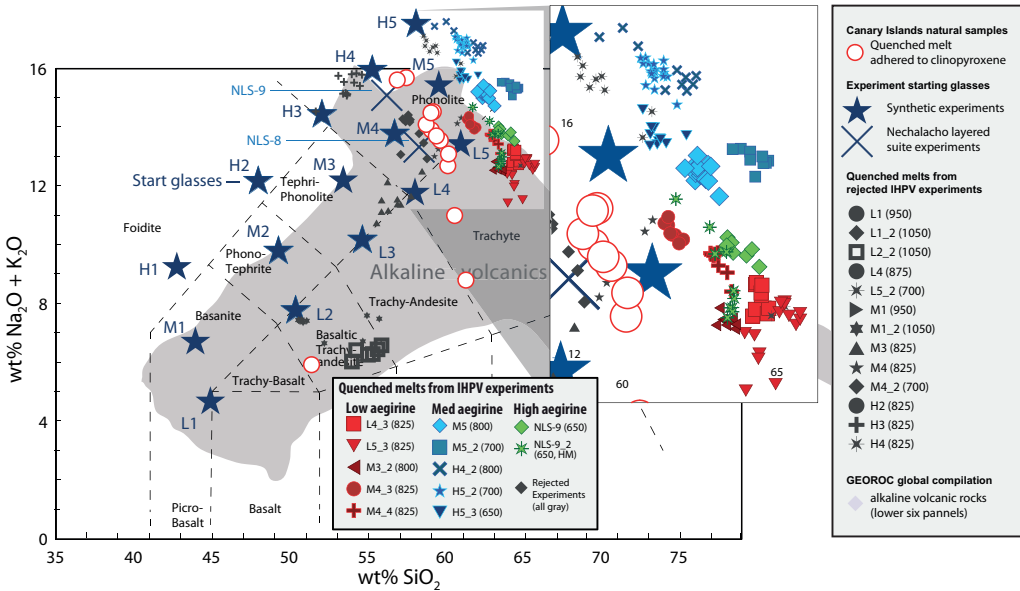


Figure S1: Total alkalies vs. silica diagram for glasses produced in internally heated pressure vessel experiments and adhered to Canary Islands clinopyroxene phenocrysts (Le Bas et al., 1986). Large stars indicate synthetic starting glass compositions as used in internally heated pressure vessel experiments (Table 1), whereas large crosses indicate the composition of powdered natural samples from the Nechalacho layered suite, NT, Canada that were used as starting materials for some experiments. The gray field indicates the compositional range expressed by alkaline volcanic provinces from around the world, sourced from the GEOROC database. Rejected experiments in dark gray are not discussed in the main text, and either did not produce clinopyroxene, produced crystals that were too small for analysis by LA-ICP-MS, or grew crystals during quench, hence preserving disequilibrium partitioning behaviour. Further diagrams showing major-element compositions for the quenched melts and the starting glasses are in Fig S2.

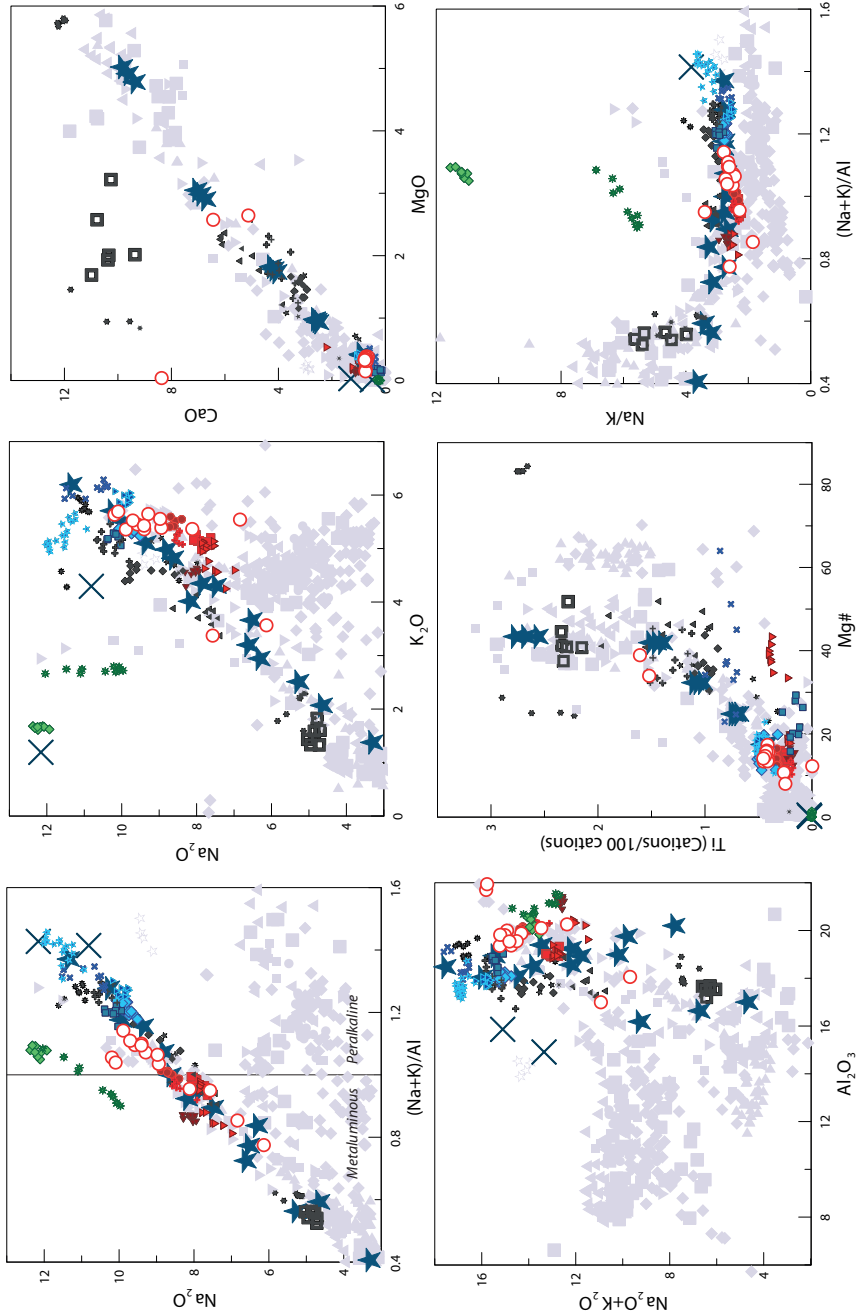


Figure S2: Major-element compositions for glass produced in the internally heated pressure vessel experiments and adhered to clinopyroxene phenocrysts from the Canary Islands. Symbols as in Fig. S1.

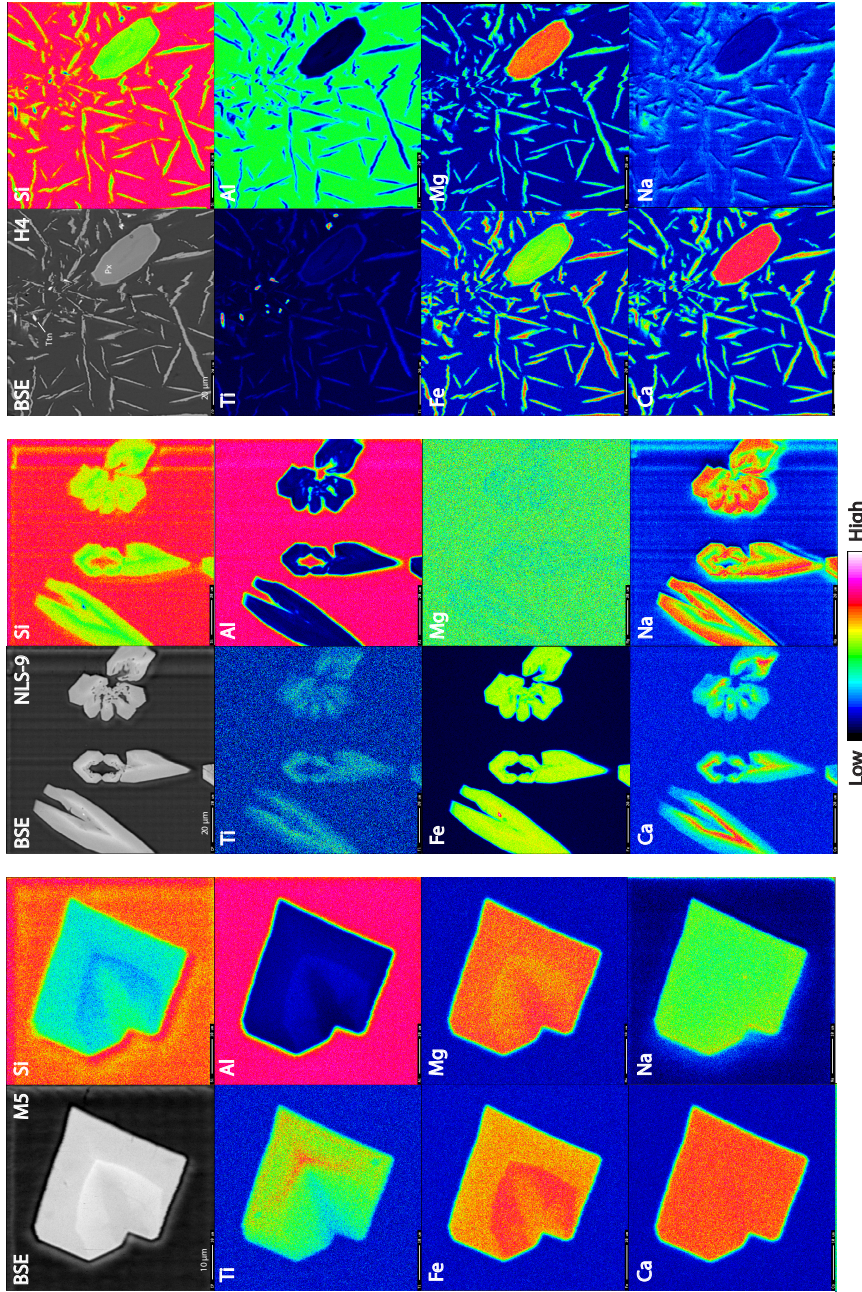


Figure S3: Element maps of clinopyroxene from internally heated pressure vessel experiments. M5 clinopyroxene have a sharp internal boundary that reflects feldspar saturation and are subtly zoned. NLS-9 clinopyroxene are more strongly zoned with swallowtail and hopper textures and rare inclusions of magnetite (cf. Walker et al., 1976; Lofgren, 1989; Shea and Hammer, 2013). H4 clinopyroxene ( $P_X$ ) display a bimodal crystal size distribution and occur with titanite (Tn). The bimodal crystal size distribution is due to a temperature perturbation during run, and renders this experiment unsuitable for this element partitioning study.

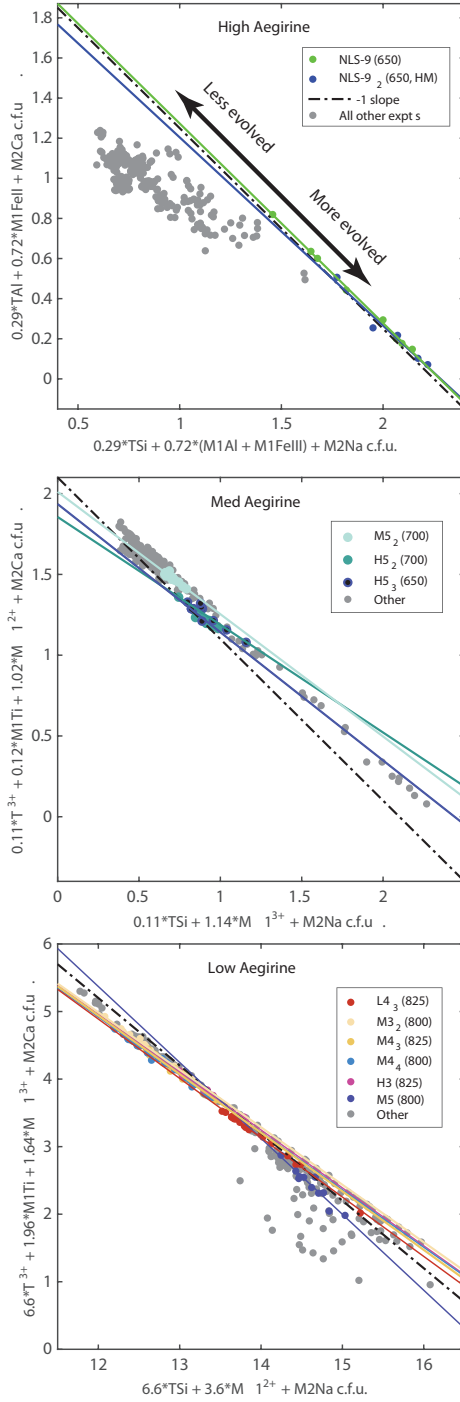


Figure S4: Major-element exchange mechanisms for (a) high, (b) medium and (c) low-aegirine clinopyroxene generated in internally heated pressure vessel experiments. Each individual plotted point represents an electron-microprobe analysis. Iron in the clinopyroxene was assigned to 2+ or 3+ valence following Droop (1987), then major-element cations were assigned to sites following Morimoto (1989, see supplement S5). Axes were defined by linear regressions between site-assigned major-element abundances, which have been checked for consistency in total site-occupancy and for charge.

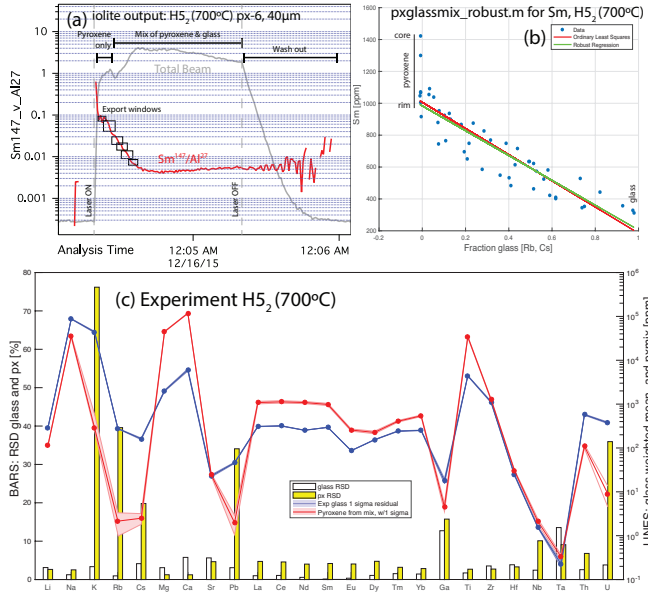


Figure S5: An example of the robust regression data reduction scheme for laser-ablation ICP-MS analyses of glass and clinopyroxene mixtures. (a) Time series of laser-ablation data, showing traces for Sm/Al (red) and total beam intensity (gray). The laser beam often ablated through the small clinopyroxene crystals, returning a mixed signal that was exported from the iolite data reduction software in short time windows as shown. Data were then normalised to the sum of major-element concentrations and mixes were deconvolved using a robust regression script written in MATLAB. (b) An example output diagram for the robust regression data reduction scheme. Clinopyroxene–glass mixing ratios were constrained by strongly incompatible elements Rb and Cs. For each element, a robust linear regression was defined between the fraction of glass in the mixture and element concentration. The intercept of this regression with zero glass returned the trace-element concentrations in the clinopyroxene. Uncertainty with this technique is typically below 10 % relative (median 9.3 % at the  $1\sigma$  level). In this example, the Sm-rich core of a zoned clinopyroxene crystal is effectively rejected during data processing, and the derived Sm concentration for the clinopyroxene is therefore closer to that of the clinopyroxene rims that are in equilibrium with the adjacent quenched melt. (c) A quality control diagram output from the MATLAB data reduction scheme showing the concentrations of various elements in the glass and clinopyroxene (lines) and the uncertainty on these concentrations expressed as a relative standard deviation ( $\delta_{\text{BARS}}$ ). Derived partition coefficients ( $D_i$ ) are the mass concentration of element ' $i$ ' in clinopyroxene divided by that in the adjacent quenched melt. Residuals for the  $D_i$  values were calculated using uncertainties derived from the clinopyroxene and glass analyses to calculate minimum and maximum partition coefficients at the  $1\sigma$  level. These are reported in Table 4 and Supplement S1.

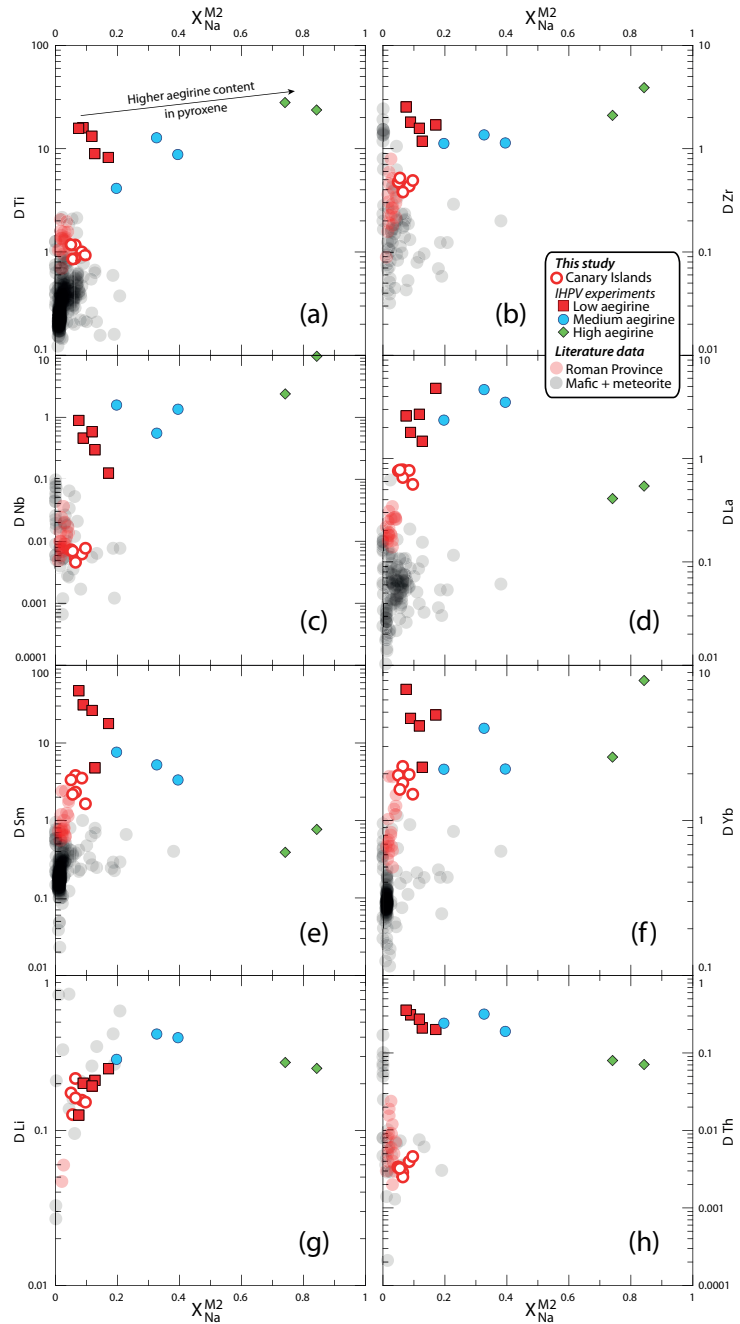


Figure S6: Element partitioning coefficients for HFSE (Ti, Zr, Nb), REE (La, Sm, Yb) and TE (Li, Th) vs.  $X_{\text{Na}}^{\text{M}2}$ . Literature values ( $n = 411$ ), including those from the Roman Province, Italy, are from the compilation of Bédard (2014).

<sub>1394</sub> **8. Electronic appendices**

xlsx

Table S1: Electronic appendix (.xlsx file) containing experiment starting glass compositions, experiment run conditions, mineral abundances in experimental charges, compositions of reference materials used for EPMA and LA-ICP analyses, major-element concentrations for experiment glasses and clinopyroxene, partition coefficients and fitted lattice-strain parameters.

kml

Table S2: Electronic appendix (.kml file) containing field locations for the Canary Islands samples.

kml

Table S3: Electronic appendix (.xlsx file) containing electron-microprobe transects across experiment clinopyroxene for Ce, Mg and Fe. The data indicate that  $D_{Ce}^{px/melt}$  values determined from our experiments are overestimates, but only by up to 25%. Sector zoning in the clinopyroxene appears to have a larger impact on apparent Ce partitioning behaviour than growth zoning.

pdf

Table S4: Electronic appendix (.pdf file) containing multiple linear regression reports from the stepwise fitting of 3+ cation lattice-strain parameters for the predictive model for element-partitioning (39 pages).

xlsx

Table S5: Electronic appendix (.xlsx file) containing a numerical model for prediction of clinopyroxene/melt element-partitioning coefficients for ions of 3+ valence. Required input data are major-element oxide compositions for clinopyroxene, pressure and temperature. The model for the M2 site is calibrated for application to systems of basaltic to peralkaline phonolite composition. The model for the M1 site is calibrated for use on alkaline to weakly peralkaline systems where the aegirine mol% in clinopyroxene does not exceed 50.

1395    **9. Supplement: Chemical heterogeneity and the approach to equi-**  
1396    **librium during the experiments**

1397    *9.1. Attainment of equilibrium in the Canary Islands rocks*

1398    The Canary Islands trace-element partition-coefficients presented here  
1399    were determined from euhedral, blade-shaped crystals free of melt inclu-  
1400    sions and chemical zonation. The corresponding quenched melt was in direct  
1401    contact with these crystals and shows no zonation in backscattered electron  
1402    images (Fig. 1). While equilibrium conditions are challenging to confirm for  
1403    a natural volcanic system, the euhedral forms, chemical homogeneity of crys-  
1404    tals, and congruency between samples from separate eruptions suggest that  
1405    the crystals grew in a stable environment, and were not subject to chemical  
1406    or physical perturbations during growth (Fig. 6).

1407    *9.2. Attainment of equilibrium in the experiments*

1408    Experiments used to determine trace-element partition-coefficients must  
1409    have attained, or at least closely approached, chemical equilibrium. Un-  
1410    fortunately no experiments are able to determine equilibrium trace-element  
1411    partition-coefficients *sensu stricto* because reversal experiments, where a  
1412    clinopyroxene re-equilibrates with a melt, are not possible owing to slug-  
1413    gish diffusion of most elements through the clinopyroxene structure (Van  
1414    Orman et al., 2001; Zhang et al., 2010). The following two sections discuss  
1415    some analytical and experimental biases that must be considered when deter-  
1416    mining mineral-melt trace-element partition-coefficients from crystallisation  
1417    experiments.

1418    *9.2.1. The formation of diffusive boundary layers*

1419    A potential barrier to chemical equilibration during crystallisation is the  
1420    formation of a diffusive boundary layer within the melt adjacent to growing  
1421    crystals. In a perfect equilibrium case there are no compositional gradients  
1422    in the melt at any time during crystal growth. However in reality the growth  
1423    of crystals depletes compatible elements from the melt and residually en-  
1424    riches incompatible elements. Theoretically, this process of crystal growth  
1425    results in formation of a (potentially ephemeral) diffusive boundary layer in  
1426    the melt directly adjacent to the crystal that is depleted with respect to  
1427    compatible elements and enriched with respect to those that are incompat-  
1428    ible (Lu et al., 1995). The composition of such a diffusive boundary layer  
1429    depends on both the relative enrichment or depletion of elements during the  
1430    crystallisation process, and the rate at which these elements diffuse through  
1431    the melt. Rapidly-diffusing elements with partition-coefficients close to unity  
1432    will have concentrations closest to that of the bulk melt.

1433    Experiments designed to investigate trace-element-partitioning behaviour  
1434    might employ slow cooling rates to limit the development of diffusive bound-  
1435    ary layers, thus forming crystals from melt that is closer in composition to  
1436    that of the bulk experiment. Such experiments then run into another prob-  
1437    lem, in that significant crystallisation may occur at temperatures above that  
1438    of the final run temperature. Rapidly-cooled experiments circumnavigate  
1439    this issue, but may form relatively more pronounced diffusive boundary layers  
1440    during crystal growth that become ‘flattened out’ during the homogenisation  
1441    stage of the experiment.

1442    Numerous diffusion data have been gathered for silicate melts over the

1443 past few decades, and a comprehensive review is given by Zhang et al.  
1444 (2010). Diffusion of trace-elements through water-saturated peralkaline melts  
1445 is rapid, owing to their depolymerised structure. For example Lanthanum  
1446 diffusion-coefficients are 6 orders of magnitude higher than for water-saturated  
1447 granitic compositions of a similar temperature (compare Rapp and Watson,  
1448 1986; Behrens and Hahn, 2009). This rapid diffusion serves to minimise the  
1449 formation of diffusive boundary layers adjacent to growing crystals in our  
1450 experiments. Coupled diffusion mechanisms complicate the application of  
1451 measured single-element diffusion-coefficients to a crystallising system (Grove  
1452 et al., 1984; Liang et al., 1994; Costa et al., 2003). Here, the diffusive flux of  
1453 trace-elements may be coupled to gradients in major-element concentration  
1454 within the melt.

1455 To investigate the impact of diffusive effects on trace-element-partitioning  
1456 between clinopyroxene and melt, Mollo et al. (2013) performed crystallisa-  
1457 tion experiments on trachybasaltic melts at a range of cooling rates (2.5–  
1458 50°C / hr). Rapid cooling rates result in depletions of Si, Ca and Mg in  
1459 the clinopyroxene that are compensated for by enrichments in Al, Na and  
1460 Ti. Regardless of cooling rate, Ounma parabolae could be fitted through  
1461 isovalent sets of partition-coefficients, indicating that crystal-lattice-effects  
1462 dominated over those associated with the formation of diffusive boundary  
1463 layers and that local equilibrium was achieved at the time of crystallisa-  
1464 tion. In their rapidly-cooled experiments Mollo et al. (2013) found apparent  
1465 clinopyroxene/melt trace-element partition-coefficients that varied with iden-  
1466 tical crystal-chemical systematics to true equilibrium partition coefficients,  
1467 the magnitude of both sets of trace-element partition-coefficients following

1468 the  $^{IV}\text{Al}$  content of the clinopyroxene (ibid., their Fig. 9). Deviations of  
1469 the partition coefficient of several orders of magnitude can be obtained only  
1470 when rapidly growing crystals entrap small portions of the diffusive boundary  
1471 layer that are found as minute melt inclusions randomly distributed in the  
1472 mineral phase (Kennedy et al., 1993). In this extreme case, partitioning be-  
1473 haviour is obviously influenced by contamination phenomena and no Onuma  
1474 parabolae can be derived. As Onuma parabolae could successfully be fitted  
1475 through partitioning data for all of our presented experiments (see following  
1476 sections), and no melt inclusions were observed in optical and electron imag-  
1477 ing, we infer that our data were not affected by the presence of such melt  
1478 inclusions, and that they may be compared directly with partitioning data  
1479 derived from experiments that employed slower cooling rates.

1480 *9.2.2. Chemical zonation in the experiment clinopyroxene: Theoretical frame-  
1481 work*

1482 Trace-elements diffuse slowly through the clinopyroxene structure relative  
1483 to that of the melt (Van Orman et al., 2001; Zhang et al., 2010), therefore no  
1484 re-equilibration of trace-elements takes place on an experimental time scale.  
1485 Strictly speaking, clinopyroxene only record true equilibrium conditions at  
1486 their outermost rim. Experiments designed for the derivation of equilibrium  
1487 partition coefficients ideally minimise bias by limiting the fraction of crystalli-  
1488 sation, producing minerals that are as homogeneous as possible. Currently  
1489 available *in situ* analytical techniques for trace-element abundances, such as  
1490 LA-ICP-MS and SIMS, are limited in terms of minimum beam-size to  $\sim 10$   
1491  $\mu\text{m}$ ; chemical zonation, however subtle, will be continuous from the core to  
1492 the rim of the mineral. Consequently, no experimentally-derived partition-

1493 coefficients record chemical equilibrium *sensu stricto*, but properly conducted  
1494 experiments may closely approximate this state.

1495 Because only the very rim of a crystal records chemical equilibrium with  
1496 the adjacent melt, and some internal portions of the minerals must be sam-  
1497 pled during *in-situ* analyses all experimentally-determined trace-element partition-  
1498 coefficients are biased toward higher values for compatible elements and lower  
1499 values for incompatible elements. The magnitude of these biases depends  
1500 on the fraction of crystallisation in the experiment, the true equilibrium  
1501 partition-coefficient of that element, as well as the proportion of each growth-  
1502 zone sampled during the *in-situ* analysis. Fortunately *in-situ* chemical anal-  
1503yses preferentially sample the mantle and rim of zoned crystals because few  
1504 analyses section a crystal perfectly through the core. As a result there is a  
1505 sampling bias toward equilibrium mineral compositions.

1506 Consider a hypothetical experimental system in which 20% of the melt  
1507 crystallises as a single mineral, and where the chemical analyses of that  
1508 mineral are truly bulk averages of that mineral composition. An incompatible  
1509 element with a true equilibrium partition coefficient of 0.1 would return a  
1510 measured partition coefficient of 0.09, a small bias because the concentration  
1511 of that incompatible element in the melt changed only subtly during the  
1512 course of crystallisation. For compatible elements with true  $D_i$  values of  
1513  $\sim 10$ , measured partition coefficients can be a factor of 2–3 higher than true  
1514 partition coefficients, because their concentration in the melt changes more  
1515 than an incompatible element during the course of crystallisation.

1516 Further complexity is introduced in systems that crystallise multiple min-  
1517erals simultaneously. In the case of experiment M3<sub>2</sub>, the REE are compatible

1518 in clinopyroxene, but are incompatible in biotite and oxides (e.g. Mahood and  
1519 Stimac, 1990; Schmidt et al., 1999). The REE have therefore been residually  
1520 enriched in the melt phase by the crystallisation of biotite and oxide miner-  
1521 als, while simultaneously being depleted from the melt by crystallisation of  
1522 clinopyroxene. These two competing processes serve to minimise the effect of  
1523 fractional crystallisation on the concentration of trace-elements in the melt  
1524 and consequently derived REE partition-coefficients between clinopyroxene  
1525 and melt will be closer to true equilibrium values.

1526 *9.2.3. Implications of the cerium zonation across the experiment clinopyrox-  
1527 ene*

1528 Electron-microprobe analyses offer a smaller minimum beam-size than  
1529 LA-ICP-MS systems at the expense of precision and of number of elements  
1530 that may be analysed simultaneously. This higher spatial resolution permit-  
1531 ted investigation of the zonation of Ce concentrations within the experiment  
1532 clinopyroxene, with Ce as a proxy for the other compatible elements.

1533 The magnitude of concentric growth zoning in the experiment clinopy-  
1534 roxene was examined by averaging bulk and rim compositions across mul-  
1535 tiple sector-zoned grains within each experiment. The median Ce counts  
1536 divided by the rim Ce counts was 1.04 for experiment M3<sub>2</sub>, 1.08 for ex-  
1537 periment M5 and 1.12 for the fluorine-bearing experiment M3-1.25F (see  
1538 Beard, 2018). Contrary to theory discussed above, the subtly (3%) crys-  
1539 tallised experiment M5 shows a greater variation in core-to-rim Ce content  
1540 than the more heavily (?? TO ADD%) crystallised experiment M3<sub>2</sub>. Further-  
1541 more, the  $D_{Ce}^{cpx/melt}$  for experiment M3<sub>2</sub> (6.2) is approximately double that  
1542 for experiment M5 (see discussion below), which should further promote the

<sub>1543</sub> formation of Cerium zonation in the clinopyroxene during crystallisation.  
<sub>1544</sub> Consequently it is possible that many existing experimentally-derived trace-  
<sub>1545</sub> element partition-coefficients are systematically offset from true equilibrium  
<sub>1546</sub> values.

<sub>1547</sub> If Cerium is used as a proxy for the behaviour of compatible elements  
<sub>1548</sub> in our experimental system, then apparent partition coefficients derived for  
<sub>1549</sub> these elements via LA-ICP-MS are systematically offset to higher values by 4–  
<sub>1550</sub> 8%. Such a systematic bias is small, relative to the variation in clinopyroxene-  
<sub>1551</sub> melt partition coefficients within our sample set, as well as in the literature.  
<sub>1552</sub> The effect of crystal zonation on incompatible element concentrations was  
<sub>1553</sub> not measured, but as outlined in the theoretical framework above, this effect  
<sub>1554</sub> should be smaller than that for the compatible elements. No correction factor  
<sub>1555</sub> has been applied to the data presented in the figures below, or in Tables 4  
<sub>1556</sub> and S1.